

AD-A283 705



NAVAL POSTGRADUATE SCHOOL
Monterey, California



94P
94-28012



DTIC
ELECTE
AUG 31 1994
S G D

THESIS

**Design, Validation and Prototype Testing of a High
Resolution All-Reflection Michelson
Interferometer for Solar Occultation
Measurements of the OI 1304-Å Triplet Emission**

by

Michael W. Gill

June, 1994

Thesis Advisor:

David D. Cleary

Approved for public release; distribution is unlimited

DTIC QUALITY INSPECTED 1

94 8 30 024

Unclassified

SECURITY CLASSIFICATION OF THIS PAGE

REPORT DOCUMENTATION PAGE

1a. REPORT SECURITY CLASSIFICATION Unclassified			1b. RESTRICTIVE MARKINGS		
2a. SECURITY CLASSIFICATION AUTHORITY			3. DISTRIBUTION/AVAILABILITY OF REPORT Approved for public release; distribution is unlimited.		
2b. DECLASSIFICATION/DOWNGRADING SCHEDULE			5. MONITORING ORGANIZATION REPORT NUMBER(S)		
4. PERFORMING ORGANIZATION REPORT NUMBER(S)			7a. NAME OF MONITORING ORGANIZATION Naval Postgraduate School		
6a. NAME OF PERFORMING ORGANIZATION Naval Postgraduate School		6b. OFFICE SYMBOL (If Applicable) 33	7b. ADDRESS (city, state, and ZIP code) Monterey, CA 93943-5000		
6c. ADDRESS (city, state, and ZIP code) Monterey, CA 93943-5000		6b. OFFICE SYMBOL (If Applicable)	9. PROCUREMENT INSTRUMENT IDENTIFICATION NUMBER		
8a. NAME OF FUNDING/SPONSORING ORGANIZATION		10. SOURCE OF FUNDING NUMBERS			
8c. ADDRESS (city, state, and ZIP code)		PROGRAM ELEMENT NO.	PROJECT NO.	TASK NO.	WORK UNIT ACCESSION NO.
11. TITLE (Include Security Classification) DESIGN, VALIDATION AND PROTOTYPE TESTING OF A HIGH RESOLUTION ALL-REFLECTION MICHELSON INTERFEROMETER FOR SOLAR OCCULTATION MEASUREMENTS OF THE OI 1304-Å TRIPLET EMISSION					
12. PERSONAL AUTHOR(S) Gill, Michael W.					
13a. TYPE OF REPORT Master's Thesis		13b. TIME COVERED FROM TO	14. DATE OF REP (year, month, day) June, 1994		15. PAGE COUNT 94
16. SUPPLEMENTARY NOTATION The views expressed in this thesis are those of the author and do not reflect the official policy or position of the Department of Defense or the U.S. Government.					
17. COSATI CODES			18. SUBJECT TERMS (continue on reverse if necessary and identify by block number)		
FIELD	GROUP	SUBGROUP	Spectroscopy, Interferometer, All-Reflection Michelson Interferometer, OI 1304-Å Emission		
19. ABSTRACT (Continue on reverse if necessary and identify by block number)					
<p>A prototype All-Reflection Michelson Interferometer (AMI) was tested using two different diffraction gratings and a variety of light sources. The original design used a focusing lens, a pinhole aperture and an off-axis parabolic mirror for collimation, a plane diffraction grating and two plane mirrors to divide and recombine the light and a CCD camera to record the interference pattern. Interference patterns were recorded and analyzed in the Interactive Data Language (IDL) using Fourier transform techniques. The design was then modified to approximate an actual instrument for remote observations of the atomic oxygen 1304-Å triplet emission. The results of numerous experiments using both the original and modified instruments verified the feasibility of using the AMI as a compact, lightweight, high resolution instrument for use on sounding rocket or satellite platforms.</p>					
20. DISTRIBUTION/AVAILABILITY OF ABSTRACT			21. ABSTRACT SECURITY CLASSIFICATION		
<input checked="" type="checkbox"/> UNCLASSIFIED/UNLIMITED <input type="checkbox"/> SAME AS RPT. <input type="checkbox"/> DTIC USERS			Unclassified		
22a. NAME OF RESPONSIBLE INDIVIDUAL David D. Cleary			22b. TELEPHONE (Include Area Code) (408) 656-2828		22c. OFFICE SYMBOL Code PH/CL

DD FORM 1473, 84 MAR

83 APR edition may be used until exhausted

SECURITY CLASSIFICATION OF THIS PAGE

All other editions are obsolete

Unclassified

Approved for public release; distribution is unlimited

Design, Validation and Prototype Testing of a High Resolution
All-Reflection Michelson Interferometer for Solar
Occultation Measurements of the OI 1304-Å Triplet Emission

by

Michael W. Gill
Lieutenant, United States Navy
B.S., California Polytechnic State University, San Luis Obispo, 1983

Submitted in partial fulfillment of the
requirements for the degree of

MASTER OF SCIENCE IN PHYSICS
from the

NAVAL POSTGRADUATE SCHOOL

June 1994

Author:



Michael W. Gill


Approved By:



David D. Cleary, Thesis Advisor



D. Scott Davis, Second Reader



William B. Colson, Chairman, Department of Physics

ABSTRACT

A prototype All-Reflection Michelson Interferometer (AMI) was tested using two different diffraction gratings and a variety of light sources. The original design used a focusing lens, a pinhole aperture and an off-axis parabolic mirror for collimation, a plane diffraction grating and two plane mirrors to divide and recombine the light and a CCD camera to record the interference pattern. Interference patterns were recorded and analyzed in the Interactive Data Language (IDL) using Fourier transform techniques. The design was then modified to approximate an actual instrument for remote observations of the atomic oxygen triplet emission. The results of numerous experiments using both the original and modified instruments verified the feasibility of using the AMI as a compact, lightweight, high resolution instrument for use on sounding rocket or satellite platforms.

Accession For	
NTIS	CRA&I <input checked="" type="checkbox"/>
DTIC	TAB <input type="checkbox"/>
Unannounced <input type="checkbox"/>	
Justification _____	
By _____	
Distribution /	
Availability Codes	
Dist	Avail and/or Special
A-1	

TABLE OF CONTENTS

I.	INTRODUCTION	1
A.	THESIS OBJECTIVES	3
B.	THESIS OUTLINE	3
II.	BACKGROUND	4
A.	ATMOSPHERIC COMPOSITION OF THE EARTH	4
1.	Temperature and Composition Profiles	4
2.	Ionosphere	7
3.	Electromagnetic Wave Propagation	10
III.	THEORY	11
A.	NATURE OF LIGHT	11
B.	INTERFERENCE	12
C.	DIFFRACTION	16
D.	THE DIFFRACTION GRATING	19
E.	THE ALL-REFLECTION MICHELSON INTERFEROMETER	20
F.	THE SOLAR OXYGEN 1304-Å TRIPLET LINE PROFILES	29
G.	THE TERRESTRIAL OXYGEN 1304-Å EMISSION	31
H.	SOLAR OCCULTATION	35
IV.	EXPERIMENT	42
A.	SETUP OF AMI	42
B.	TESTING WITH MERCURY VAPOR LAMP	45

C.	TESTING WITH SODIUM VAPOR LAMP	55
D.	FINAL MODIFICATION OF AMI	65
E.	TESTING WITH ULTRAVIOLET SOURCE	70
V.	SUMMARY, CONCLUSIONS AND RECOMMENDATIONS	74
A.	SUMMARY OF FINDINGS	74
B.	RECOMMENDATIONS FOR FURTHER STUDIES	75
	APPENDIX A - IDL PROCEDURES	77
	APPENDIX B - EDC FILES	83
	LIST OF REFERENCES	84
	INITIAL DISTRIBUTION LIST	85

LIST OF TABLES

TABLE 1.	COMPARISON OF GRATINGS WITH DIFFERENT LIGHT SOURCES (Standard with $\rho=1200$, Sinusoid with $\rho=2400$)	43
TABLE 2.	PERCENTAGE COMPARISON OF GRATINGS (Standard with $\rho=1200$, Sinusoid with $\rho=2400$)	44
TABLE 3.	SODIUM DOUBLET EMISSION ANALYSIS (Summed by Rows of 2)	63

LIST OF FIGURES

FIGURE 1.	Temperature Profile of the Atmosphere	4
FIGURE 2.	Ion Production Probability	8
FIGURE 3.	Electron Density Profile	10
FIGURE 4.	Double Slit Interference	14
FIGURE 5.	Huygens-Fresnel Principle	17
FIGURE 6.	Multiple-Slit Diffraction	18
FIGURE 7.	A Diffraction Grating	19
FIGURE 8.	Michelson Interferometer	21
FIGURE 9.	All-Reflection Michelson Interferometer	22
FIGURE 10.	AMI - Reflection from Diffraction Grating	23
FIGURE 11.	AMI - Reflection from Plane Mirrors	24
FIGURE 12.	AMI - Recombination at Detector	25
FIGURE 13.	Expanded View of AMI at the Detector	26
FIGURE 14.	Minimum Resolution of AMI	27
FIGURE 15.	Solar Oxygen 1304.86-Å Emission Line Profile	31
FIGURE 16.	Comparison of Doppler and Voigt Line Profiles	35
FIGURE 17.	Simulated Oxygen 1304.86-Å Line Profile versus Column Density ($N=1 \times 10^{17}$, 1×10^{18} and 1×10^{19})	37
FIGURE 18.	Simulated Oxygen 1304.86-Å Line Profile versus Column Density ($N=1 \times 10^{21}$, 1×10^{22} and 1×10^{23})	38
FIGURE 19.	Simulated 1304.86-Å Line Profile versus Temperature	39

FIGURE 20.	Enlarged View of Line Profile versus Temperature	40
FIGURE 21.	Growth Curve for Oxygen 1304.86-Å Line	41
FIGURE 22.	Diffraction Grating Comparison Diagram	43
FIGURE 23.	Initial Interference Pattern for Mercury Vapor Lamp	46
FIGURE 24.	Interference Pattern for Mercury Vapor Lamp	49
FIGURE 25.	Interference Profile for Mercury Vapor Lamp	50
FIGURE 26.	Fourier Transform for Mercury Vapor Lamp	51
FIGURE 27.	Interference Pattern for Mercury Vapor Lamp (High Spatial Frequency)	52
FIGURE 28.	Interference Profile for Mercury Vapor Lamp (High Spatial Frequency)	53
FIGURE 29.	Fourier Transform for Mercury Vapor Lamp (High Spatial Frequency)	54
FIGURE 30.	Plot of Intensity Versus Spatial Frequency (Mercury Vapor Lamp)	55
FIGURE 31.	Interference Pattern for Sodium Vapor Lamp (λ_0 less than λ_1 and λ_2)	57
FIGURE 32.	Interference Profile for Sodium Vapor Lamp (λ_0 less than λ_1 and λ_2)	58
FIGURE 33.	Fourier Transform for Sodium Vapor Lamp (λ_0 less than λ_1 and λ_2)	59
FIGURE 34.	Interference Pattern for Sodium Vapor Lamp (λ_0 between λ_1 and λ_2)	60
FIGURE 35.	Interference Profile for Sodium Vapor Lamp (λ_0 between λ_1 and λ_2)	61
FIGURE 36.	Fourier Transform for Sodium Vapor Lamp (λ_0 between λ_1 and λ_2)	62
FIGURE 37.	Comparison of Sodium Doublet Emission Profiles (Intensity Profile Summed Over 1, 4, 16, 64 and 244 Rows)	65
FIGURE 38.	Front View of AMI	67
FIGURE 39.	Rear View of AMI	68
FIGURE 40.	Interference Pattern after Final Modifications to AMI	70

I. INTRODUCTION

Knowledge of the chemistry and composition of the earth's upper atmosphere is of vital importance to many academic and government activities. Specifically, an understanding of the electron density profile of the ionosphere has direct application to military over-the-horizon radar systems and high frequency radio communications. Understanding the thermosphere is also important to the scientific community in areas ranging from accurate prediction of weather patterns to the study of terrestrial planets and comets.

Atomic oxygen is a major constituent of the upper atmosphere of the earth and, because it is highly reactive, plays a central role in the photochemistry of the ionosphere. It is formed naturally in the thermosphere by the photo-dissociation and electron-impact dissociation of molecular oxygen. Employing a variety of methods, the density of atomic oxygen in the thermosphere has been measured on numerous occasions, but the results differ widely and the absolute concentration of atomic oxygen has proven notoriously difficult to establish.

A relatively new technique for measuring atomic oxygen in the thermosphere under research at the Naval Postgraduate School (NPS) involves using the solar occultation of the OI 1304-Å emission to infer the terrestrial atomic oxygen density. This technique is unique because it is insensitive to many of the sources of uncertainty that have affected previous measurements. The OI 1304-Å triplet is a prominent emission in both the solar spectrum and terrestrial airglow. Any observation of the solar OI 1304-Å line profile from within the atmosphere will be absorbed to some degree by the intervening column of oxygen and the extent of this attenuation can be used to determine the column density of the oxygen.

For space flight observations, high resolution measurements are made almost exclusively with Michelson or Fabry-Perot interferometers rather than grating spectrometers. Emissions at wavelengths of 1304-Å fall into the far ultraviolet (FUV) portion of the spectrum. The number of window materials in the FUV is very limited and, as a result, Fabry-Perot and standard Michelson interferometers are extremely difficult to build. Therefore, instruments utilizing all-reflection interferometers are needed for this portion of the spectrum.

The NPS Physics Department has been actively involved in ionospheric research for several years. They have conducted three successful sounding rocket experiments using an instrument called the Middle Ultraviolet Spectrograph (MUSTANG). MUSTANG observes emissions in the range from 1800-Å to 3400-Å with a resolution of approximately 10-Å. The successor to MUSTANG is the higher resolution Ionospheric Spectroscopy And Atmospheric Composition (ISAAC) instrument, scheduled for launch in 1995 aboard a low earth orbit satellite. ISAAC is expected to have a resolution of 2.5-Å.

During MUSTANG development it became evident that an instrument providing even higher wavelength resolution, on the order of a few mÅ, was necessary to permit the investigation of radiation transport through the examination of optically thick lines. Nichols (1990) designed and built a prototype interferometer using all-reflective optics and a spherical grating. The design was validated using a green He-Ne laser in the laboratory (Cleary et al., 1992). Wallace (1992) found that a similar instrument based on a plane diffraction grating is more suitable because it produces linear interference fringes which are more amenable to analysis using Fourier transform techniques. He designed and built the All-Reflection Michelson Interferometer (AMI). Validation of the design using the DART ray tracing program was

performed by Carlson (1993) and developmental testing was begun by Risley (1993). This thesis is a continuation of that work.

A. THESIS OBJECTIVES

The main objective of this thesis is to continue developmental testing of the AMI using visible light sources in the 5000 to 6000-Å range and incoherent light sources with wavelengths in the 2000 to 3000-Å range. The ultimate goal is to demonstrate the feasibility of the AMI for analyzing the solar occultation of the OI 1304-Å triplet emission to determine the density of atomic oxygen in the thermosphere so that development of a practical instrument for space flight measurements can begin.

B. THESIS OUTLINE

This thesis is divided into five sections. The first section is the introduction of the thesis. Section II provides background information on the composition of the atmosphere and the dynamic processes that produce the emission profiles of interest. The theory of Section III includes a brief review of interference and diffraction, an introduction to the AMI and solar occultation. Section IV describes the experiments conducted and data collected from the various instruments, and Section V presents the results of the research and provides recommendations for further study. Appendices are also included which contain IDL procedures used to store and to analyze the data and EDC files used to generate some of the figures.

II. BACKGROUND

This section provides general information relating to the physical processes and dynamics which control the composition of the earth's atmosphere. It also provides the motivation which led to the development of a high resolution FUV interferometer.

A. ATMOSPHERIC COMPOSITION OF THE EARTH

1. Temperature and Composition Profiles

The earth's atmosphere can be described as a series of stacked horizontal layers based on kinetic temperature or chemical composition. The temperature and composition distributions of the atmosphere are illustrated in Figure 1.

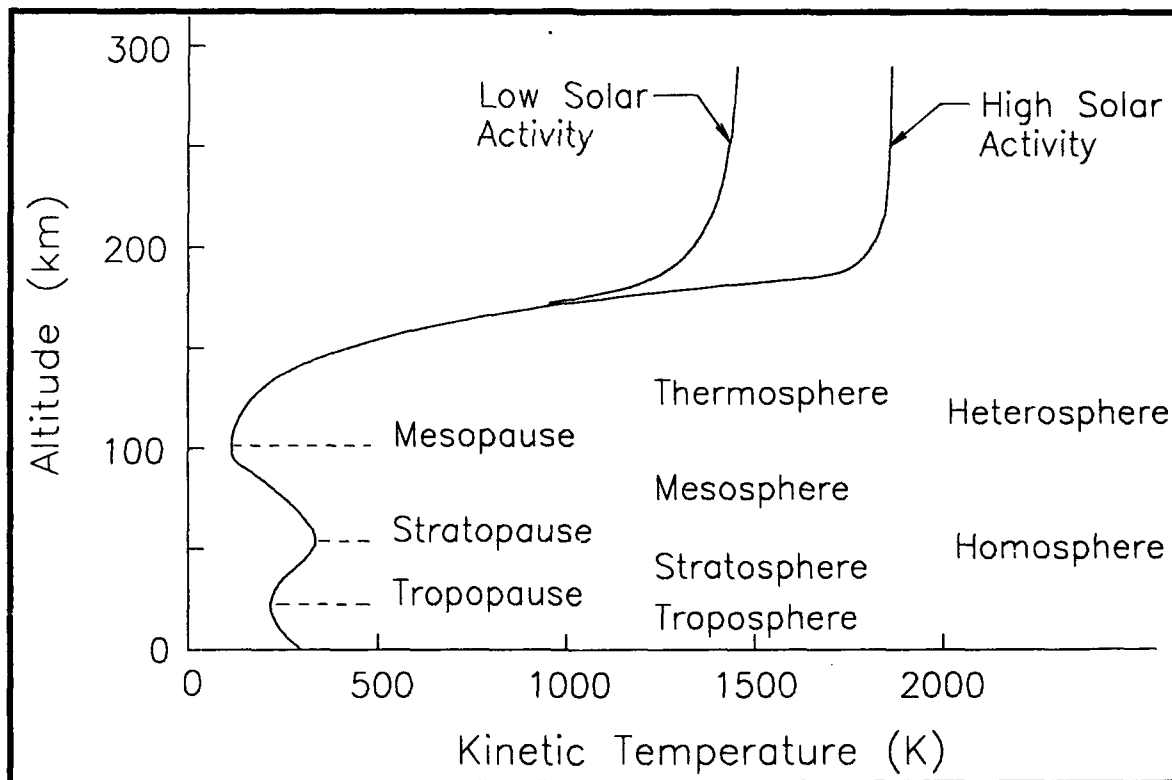


Figure 1 Temperature Profile of the Atmosphere

The atmosphere is divided into four different regions or "spheres" based primarily on the variation of temperature with altitude above the earth's surface. The different regions in order of ascending altitude are: the troposphere, the stratosphere, the mesosphere and the thermosphere. Each of these spheres is separated by a transition region or "pause" where the derivative of temperature with respect to altitude goes to zero. The three transition regions separating the four characteristic layers are the tropopause, the stratopause and the mesopause.

The troposphere (0-10 km) is the layer of the atmosphere where clouds and weather originate. In this region, the dominant physical process is Eddy mixing and the surface of the earth is the primary source of warming. As a result, the temperature decreases at a fairly uniform rate (commonly referred to as the lapse rate) of -6.5 K/km and reaches a minimum of approximately 210 K at the tropopause (10 km).

The next region of the atmosphere is the stratosphere (10-50 km), where the temperature increases with increasing altitude due to the absorption of solar ultraviolet radiation. This effect is especially true in the ozone layer (30 km) where a concentration of a few parts per million of O_3 leads to very pronounced absorption of wavelengths in the 2000-3000-Å range and subsequent heating of the atmospheric gases. The positive temperature gradient observed in the stratosphere terminates at the stratopause (50 km).

The third layer is called the mesosphere (50-80 km) which is characterized by a negative temperature gradient. The temperature in this region is determined mostly by convection, the warmer stratosphere now acting in much the same way as the planetary surface acts with respect to the troposphere. The cooling trend observed in the mesosphere ceases at the mesopause (80 km), the coolest region of the atmosphere, where the temperature is approximately 180 K.

The final region of the atmosphere is the thermosphere (above 80 km), which displays a positive temperature gradient due primarily to the absorption of electromagnetic radiation by molecular oxygen in the range of $\lambda < 2000\text{-}\text{\AA}$. Since the heating now occurs from above, there is no convection, and the temperature increases until it reaches a maximum of approximately 1600 K at altitudes of 300-400 km. Above 400 km the atmosphere is essentially isothermal. As Figure 1 shows, the high temperatures found in the upper reaches of the atmosphere display considerable variation (900-1800 K) depending on the amount of solar activity and time-of-day. These variations are a result of the low heat capacity of the upper atmosphere. Fluctuations in the amount of UV radiation are rapidly reflected in temperature changes. In the thermosphere, interaction between solar radiation and atmospheric gases form the region of ionized particles known as the ionosphere. This region is of primary interest for applications discussed in this thesis.

If the atmosphere is divided according to composition there are three characteristic spheres: the homosphere, the heterosphere and the exosphere. In the homosphere (0-100 km), the composition of the atmosphere is essentially uniform in the sense that the mean molecular weight remains constant. The primary transport mechanism in this region is eddy diffusion, a turbulent mixing which keeps the relative concentrations of component gases effectively constant.

Above the homosphere lies the heterosphere (100-500 km), where the primary transport mechanism is molecular diffusion. Very little vertical mixing occurs in this region, and the molecules tend to separate based on differences in molecular weight.

Finally, the exosphere (above 500 km) identifies the layer where collisions between atoms become extremely infrequent. Because of the infrequency of collisions, particles

have high kinetic energies, and the escape of molecules from the atmosphere becomes significant.

2. Ionosphere

The ionosphere (50-1000 km) encompasses the upper part of the homosphere, the heterosphere and the lower region of the exosphere. The relative lack of vertical mixing in this layer, combined with an increasing flux of solar photons results in the formation of a partially ionized plasma. Although electrically neutral as a whole, the atmosphere in this region is comprised largely of long-lived positive ions and free electrons. Due to the large difference in mass between an ion and electron (the ions can be 50,000 times as massive as the electrons), the electrons are much more mobile. Hence, it is primarily the free moving electrons which interact with electromagnetic waves in the ionosphere. By accurately measuring electron density profiles the electromagnetic properties of the ionosphere can be inferred and exploited tactically by the military.

The primary source of free electrons in the atmosphere is photoionization, where an incident solar photon strikes a neutral atom or molecule, forming a positive ion and a free electron. The process can be described by the equation



where M is any molecule (or atom) and $h\nu$ is the photon energy. The rate of this reaction depends on the product of the concentration [M] and the flux of photons [$h\nu$]. At high altitudes there is a large flux of photons but very few particles, and at low altitudes the reverse is true, so that the electron production function peaks at some intermediate level. In 1931, Chapman devised a simplified theoretical model of this process by assuming the atmosphere was comprised of only one constituent. Despite this rather drastic simplification, the theory yields

remarkably good results. Since each dominant atmospheric species has its own ionization potential and reaction rate, the actual atmosphere can be represented by the superposition of a number of Chapman layers. A typical Chapman profile is shown in Figure 2.

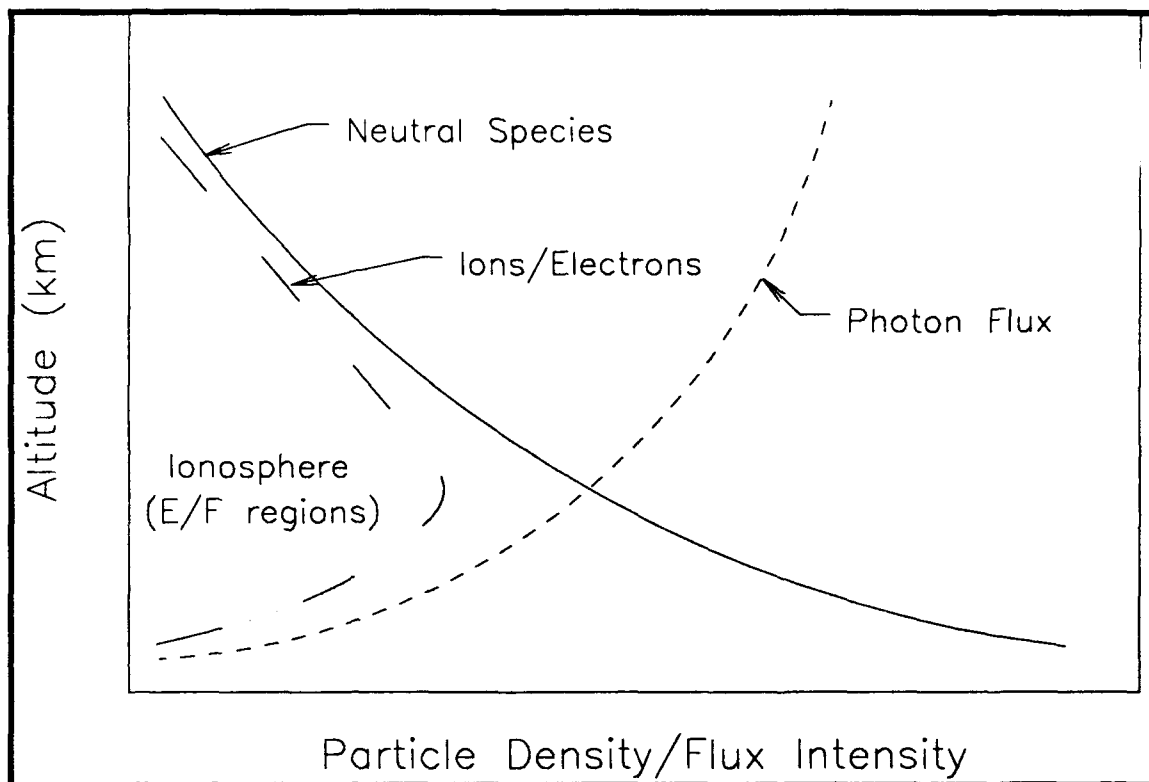


Figure 2 Ion Production Probability

Different molecules absorb at different wavelengths, and the flux of photons at a particular wavelength varies with altitude. In the EUV high energy, short wavelength photons generally penetrate farther into the atmosphere than long wavelength photons. The relative densities of different molecules also vary with altitude, and these effects combine to divide the ionosphere into four layers (D, E, F1 and F2) based upon relative maxima in the electron density profile. These layers vary with time of day, geographic location and solar activity.

The D layer (50-90 km) is the lowest region of the ionosphere and is produced by the penetrating component of the incident radiation, primarily the ionization of nitric oxide by the solar Lyman- α emission at a wavelength of 1216-Å. At night, when there is no incident radiation, the electrons and ions quickly recombine and the layer disappears, except at auroral and polar latitudes.

The next region, the E layer (90-140 km), is formed predominantly from the ionization of molecular oxygen by incident ultraviolet light and soft X-rays from the sun. Like the D layer, the E layer disappears at night except at latitudes above 60° where particle bombardment tends to maintain the ionization.

The final region is broken down into two layers, the F1 (140-200 km) and the F2 (above 200 km). The F1 layer is really a ledge in the electron density profile at the bottom of the F2 layer. It occurs only during daylight hours and is most pronounced during the summer months and at times of high solar activity (sunspot maximum). The presence of the F1 ledge can be attributed to the ionization of molecular oxygen. The F2 layer has the highest electron density and is present during the day and at night. As with the F1 layer, the F2 predominates during the daylight hours and summer months. However, unlike the F1 region, the F2 persists at night because the density of particles is so low that collisions leading to the recombination of electrons and ions are extremely rare. A plot of typical electron densities versus altitude for both daytime and nighttime conditions is shown in Figure 3.

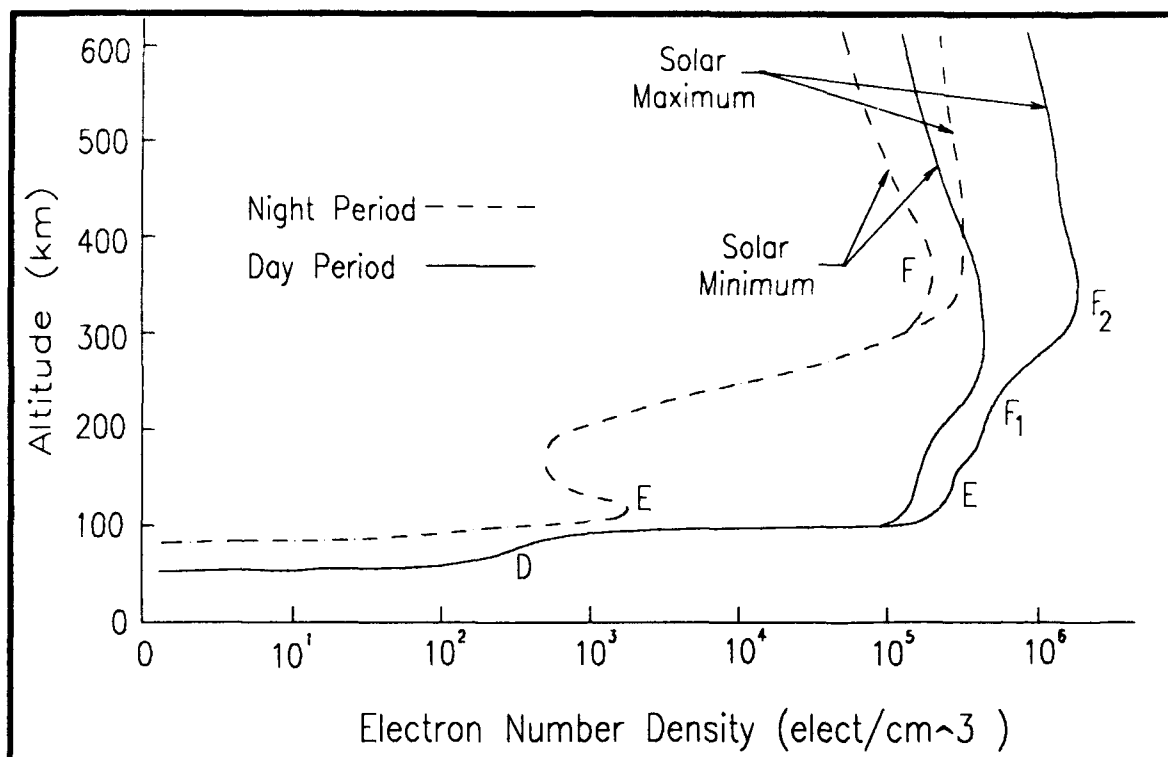


Figure 3 Electron Density profile

3. Electromagnetic Wave Propagation

The ionospheric influence on radio wave propagation is significant and is the basis for a great deal of study. The radio frequency (RF) atmospheric window ranges from 10 MHz-20 GHz. Due to their interaction with electrons, radio wave frequencies must be higher than the "plasma frequency" in order to pass through the atmosphere and reach a satellite or probe. The plasma frequency is the natural oscillation that electrons have in a magnetic field. For OTHR and "skip" communications, the frequency must be below the plasma frequency so that reflections of radio waves will occur. An ability to distinguish between propagation modes under a variety of circumstances establishes the requirement for an accurate electron density "map" of the ionosphere.

III. THEORY

This section introduces the basic theory required to understand the method, results, discussion and conclusions regarding the AMI. First a general overview of interference and diffraction theory is presented. For a more detailed presentation on interference and diffraction theory refer to any standard text on basic physics, electromagnetic theory or optics, such as Hecht (1987) or Möller (1988). This is followed by a description of the AMI, solar line profiles, specifically the oxygen 1304-Å emission, solar occultation and a short description of the mathematical equations used to model the line profile of interest.

A. NATURE OF LIGHT

The work of Maxwell and others has shown that light is electromagnetic in nature, and classical electrodynamics points to the idea of a continuous transfer of energy by way of electromagnetic waves. Quantum electrodynamics, on the other hand, describes electromagnetic interactions and the transport of energy in terms of massless elementary particles known as photons, which are localized, propagating quanta of electromagnetic energy. This dual nature of light is evidenced by the fact that it propagates through space in a wave-like fashion and yet can display particle-like behavior during emission and absorption processes.

If the wavelength of light is small in comparison to the size of an instrument's optics, the techniques of geometrical optics may be used. A more precise treatment, applicable when the dimensions of the apparatus are small, is that of physical optics. In physical optics the dominant property of light is its wave nature.

B. INTERFERENCE

Interference is a consequence of the wave nature of light and can be described as the phenomena that occurs when light rays combine. The intensity of the resultant wave may be zero at certain positions, creating dark fringes and an interference pattern.

Light waves can be considered as vector quantities comprised of two transverse vector components propagating together, the electric field and the magnetic field. The irradiance I , which is proportional to the time average of the magnitude of E squared ($E \cdot E^* = \langle E^2 \rangle$), is of primary interest for most optics applications because it, or some quantity generated by it, is typically sensed by the optical detectors.

Consider two coherent plane waves of equal magnitude, emanating from the same source and represented by their vector components E_1 and E_2 . The complex representation of these waves traveling in the positive x direction are

$$E_1 = Ae^{-i(kx - \omega t)} \quad (2)$$

$$E_2 = Ae^{-i(kx - \omega t + \phi)}, \quad (3)$$

where A is the amplitude, ω is the wave frequency, k is the propagation vector ($k=2\pi/\lambda$) and ϕ is the phase shift between the two waves. A plane of constant phase that is perpendicular to the direction of propagation is called a wavefront. According to the principle of superposition, the electric field intensity E , at a point in space arising from the separate fields E_1 and E_2 , is given by

$$E = E_1 + E_2 = Ae^{-i(kx - \omega t)}(1 + e^{-i\phi}). \quad (4)$$

The last term may be rewritten as

$$1 + e^{-i\phi} = e^{-i\frac{\phi}{2}} \left(e^{-i\frac{\phi}{2}} + e^{i\frac{\phi}{2}} \right) = 2e^{-i\frac{\phi}{2}} \cos\left(\frac{\phi}{2}\right), \quad (5)$$

and the irradiance becomes

$$I = E \bullet E^* = 4A^2 \cos^2\left(\frac{\phi}{2}\right), \quad (6)$$

where the term $2A \cos\left(\frac{\phi}{2}\right)$ is called the amplitude factor. It is evident from equation (6) that the time dependence is automatically eliminated when calculating the irradiance, and I depends only on the square of the amplitude factor.

In many experiments, relative intensity measurements are recorded, and the irradiance can be described by

$$I = I_0 \cos^2\left(\frac{\phi}{2}\right), \quad (7)$$

where I_0 is the reference intensity. Constructive interference occurs when the absolute value of the amplitude factor is a maximum, and destructive interference takes place when this factor is zero. In other words, constructive interference takes place where $\phi=2m\pi$ and destructive interference where $\phi=(2m+1)\pi$, for any integer m .

Interference of light waves from different sources is the periodic enhancement and reduction of the irradiance of the superimposed waves. It is caused either by the propagation path length difference or an explicit phase shift between the waves or both. Interference theory can be extended to any number of superimposed waves, not just the two wave interference example used in the above derivation.

The interference of light waves can be produced by splitting a single wavefront into two waves which travel different paths. Double-slit interference is an example of this and was first demonstrated by Young in 1802. Monochromatic, collimated light is allowed to strike an opaque screen which contains two small slits a short distance apart, and the resultant pattern is viewed

on a second screen some distance away from the first screen. An illustration of this is depicted in Figure 4. In this figure, y is the distance between the slits, x the distance from the slits to the detector, θ the angle between the centerline and the observation point P and d the difference in distance between optical paths.

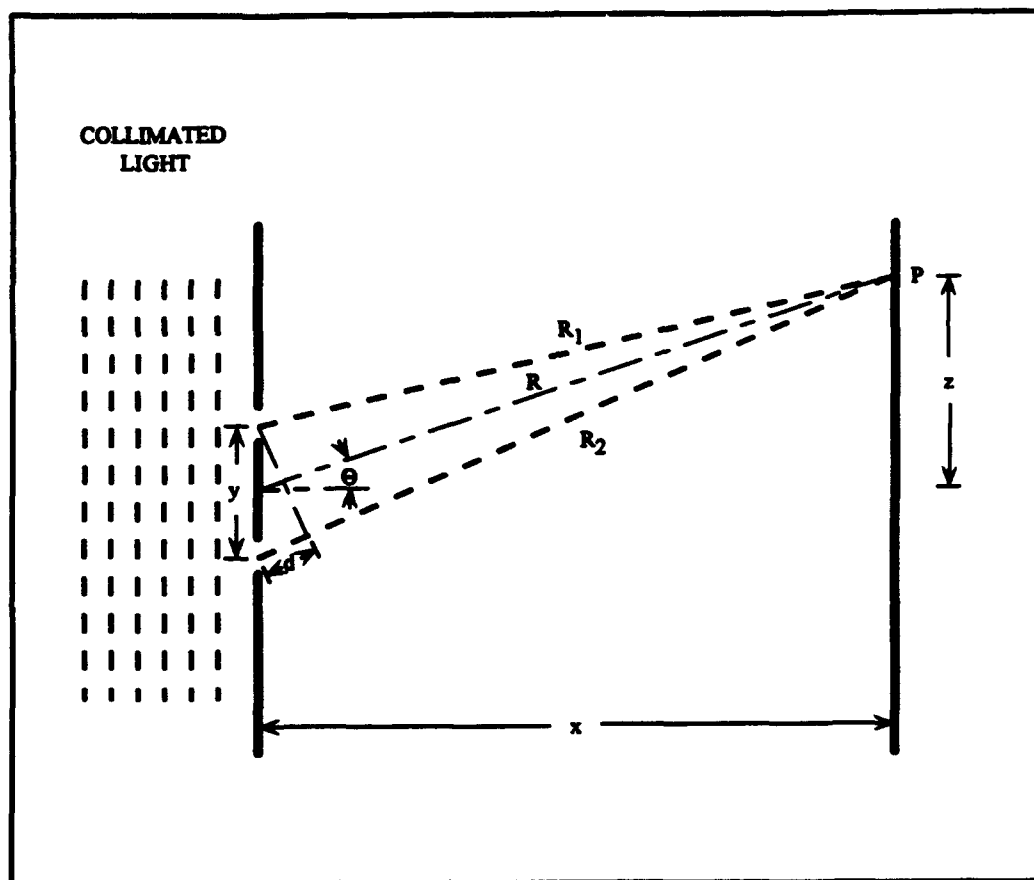


Figure 4 Double-Slit Interference

Since the light is monochromatic, the propagation vector for the wave leaving each slit has the same magnitude, $2\pi/\lambda$. The electric field at P is the superposition of the fields coming from each slit at that point, and the irradiance can be described by Equation (7). Assuming the detector is a large distance from the slit, the path difference can be approximated by $d \approx y \sin \theta$, and the phase shift between the separate waves becomes

$$\phi = \left(\frac{2\pi}{\lambda} \right) y \sin \theta . \quad (8)$$

Substitution of Equation (8) into Equation (7) gives an irradiance at P of

$$I = I_0 \cos^2 \left(\frac{\pi y \sin \theta}{\lambda} \right). \quad (9)$$

From Equation (9) it is evident that I is a maximum when the optical path difference is an integer multiple of λ and a minimum when the path difference is a half integer multiple of λ . By restricting the observation point on the detector to a small area around the optical axis such that the off-axis distance $z \ll x$, $\sin \theta$ can be approximated by θ ($\sin \theta \approx \theta \approx z/x$). Equation (9) then reduces to

$$I = I_0 \cos^2 \left(\frac{\pi y z}{\lambda x} \right), \quad (10)$$

and the detection screen will display equally spaced bright fringes separated by a distance of

$$\Delta z = \left(\frac{\lambda x}{y} \right). \quad (11)$$

The intensity of the double-slit interference pattern will decrease as z increases for two reasons. The first deals with the initial assumption of infinitesimally narrow slits radiating uniformly in all directions. Due to diffraction effects, however, light does not radiate uniformly but decreases to zero for large values of θ . Diffraction is discussed in more detail in the next section.

The second reason the intensity of the pattern falls off to zero is the concept of coherence length. Light does not travel through a medium as a perfect, continuous sinusoid but instead as wave groups that appear approximately as sinusoids for some specific length, defined as the coherence length. This is described as a photon wavetrain. The importance of coherence lies in

the fact that for interference to take place, paired groups of similar wavetrains must arrive almost simultaneously at P. If the path length difference is greater than the coherence length, wavetrains do not arrive within the coherence time, and interference does not occur. For light sources such as lasers the coherence length can be long (≈ 1 m), and the interference pattern is easy to produce. For most natural light sources such as incandescent lamps and discharge tubes, which show no particular coordination between emitting atoms, the coherence length is short, and the interference pattern can only be generated with very small optical path differences. That is the reason interference patterns are much easier to produce with laboratory lasers.

C. DIFFRACTION

Diffraction is a general characteristic of wave phenomena and occurs whenever a portion of a wavefront (sound, matter or light) is obstructed in some way. The distinction between interference and diffraction is somewhat artificial, but it is customary to speak of interference when considering the superposition of a few waves, and diffraction when referring to a large number of waves. The mathematical analysis of this phenomena is generally treated by one of two approximations: Fresnel, or near-field diffraction, and Fraunhofer, or far-field diffraction. Fresnel diffraction occurs when the plane of observation is in close proximity to the obstruction, and Fraunhofer diffraction when the observation plane is a large distance from the obstruction. This thesis deals with far-field diffraction of light waves, so only Fraunhofer diffraction of light waves will be discussed.

Diffraction effects are a consequence of Huygens-Fresnel principle, which states that every unobstructed point of a wavefront serves as a source of spherical secondary wavelets. The amplitude of the field at any point beyond the obstruction is the superposition of these wavelets, in both amplitude and phase. An illustration of Huygens-Fresnel principle is depicted in Figure

5. As shown in the diagram, light traveling through the central portion of the aperture continues to propagate in the same direction, but light passing by the edges of the aperture bends around the obstruction and propagates in a different direction. Near the aperture, the resulting waves appear as plane waves with slightly curved edges. When viewed farther away, however, the wavefronts become spherical.

If the single aperture of Figure 5 is replaced by a number of slits, the interference phenomena described in the previous section are superimposed on the diffraction pattern from each of the slits. The resulting pattern is a series of alternately spaced light and dark fringes. This is pictured in Figure 6.

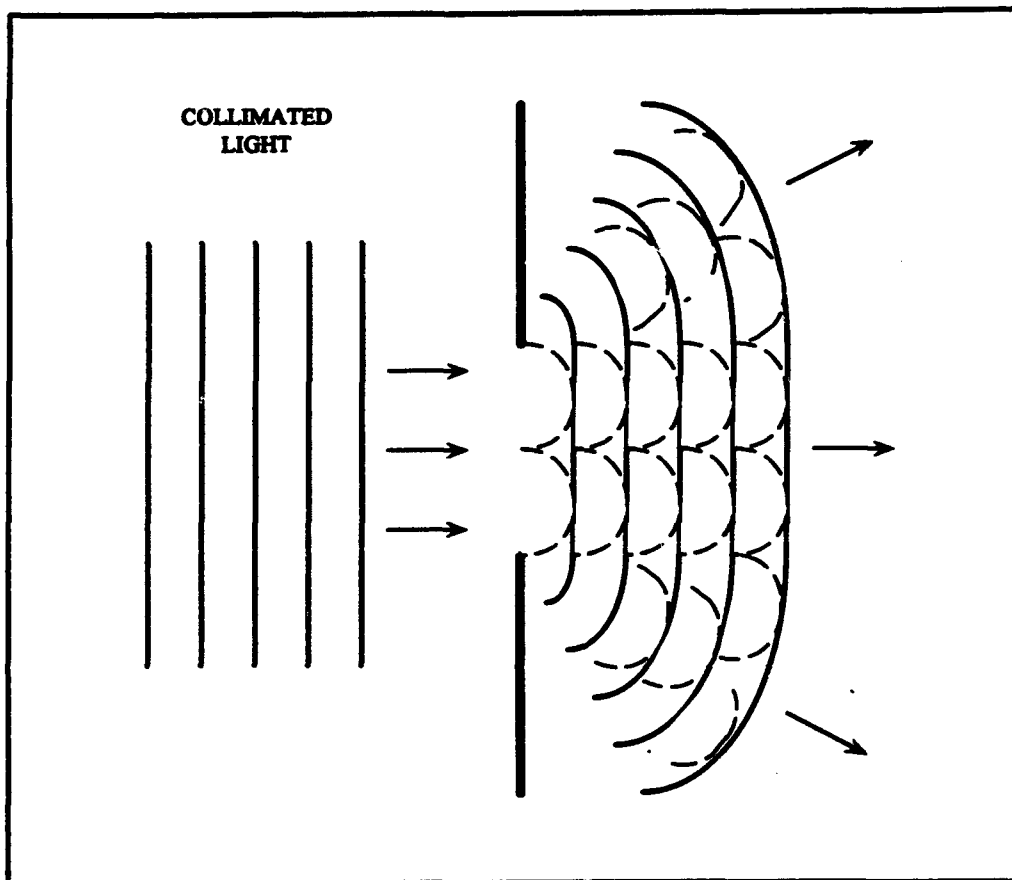


Figure 5 Huygens-Fresnel Principle

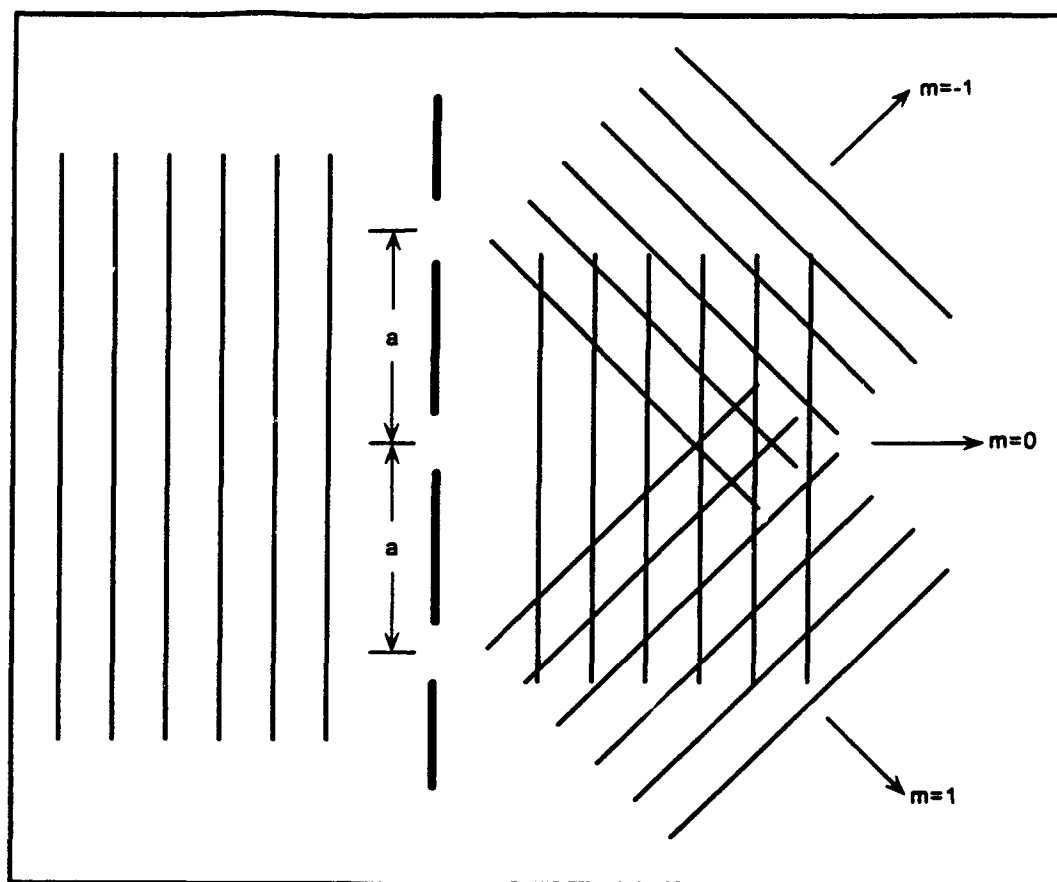


Figure 6 Multiple Slit Diffraction

The intensity of the bright fringes is a maximum at the center of the pattern and drops off to zero as the distance from the optical axis increases. The overall effect is to create a number of different directions where constructive interference occurs. These are termed diffraction orders and are designated by $m=-1, 0, 1$, etc., depending on their direction.

The equation describing the relationships of Figure 6 is called the grating equation and is defined as

$$m\lambda = a \sin\theta_m, \quad (12)$$

where m is the diffraction order, λ is the wavelength, a is the distance between slits and θ_m the deflection angle measured from the grating normal. For a source with a broad continuous

spectrum, the $m=0$ order image corresponds to the unaltered, $\theta_0=0$, white-light view of the source. Since Equation (12) is dependent on λ , any value of $m \neq 0$ results in a number of colored beams diffracted at slightly different angles.

D. THE DIFFRACTION GRATING

A diffraction grating is a repetitive array of diffracting elements, such as slits, that alters the phase or amplitude of a wave. The effect of a diffraction grating is very similar to a multiple slit arrangement, and the properties of the grating can be described using a modified version of the grating equation. Figure 7 shows a diagram of a typical reflecting diffraction grating.

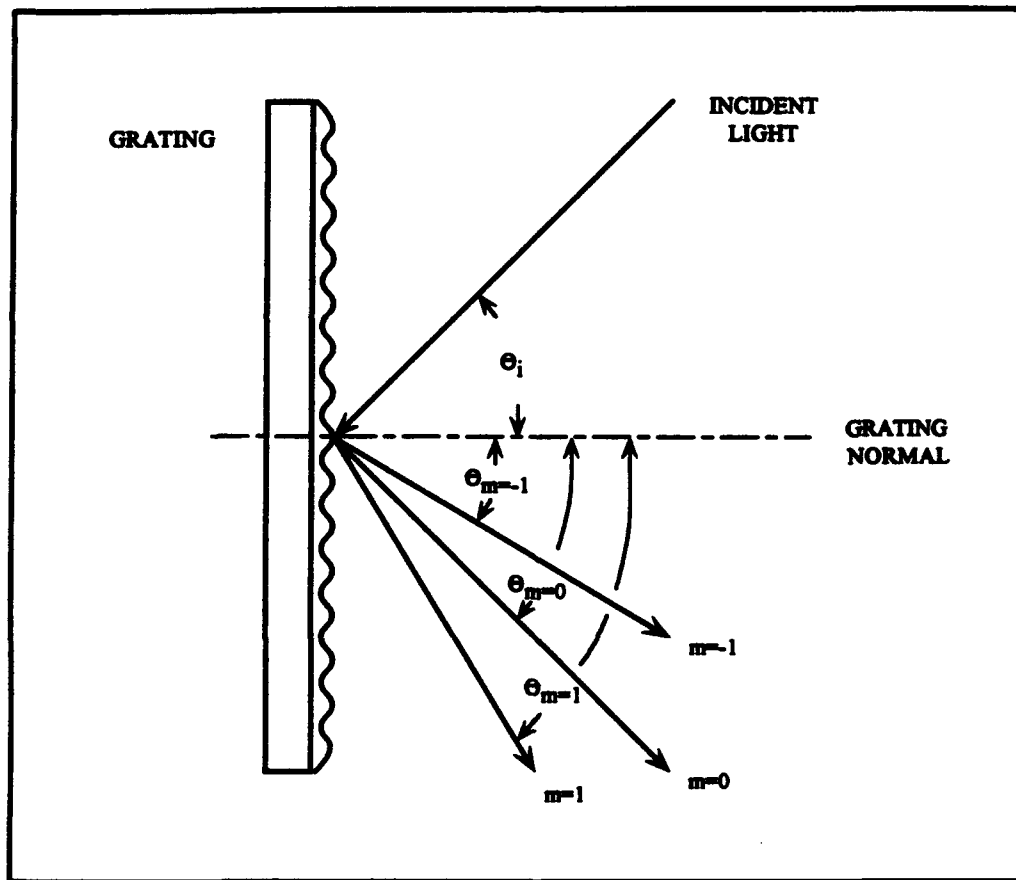


Figure 7 A Diffraction Grating

For this arrangement, the grating equation becomes

$$m\lambda = a(\sin\theta_m - \sin\theta_i), \quad (13)$$

where a and m are defined as in Equation (12), θ_i is the angle of incidence and θ_m is the diffraction angle for that order. θ_m is measured clockwise from the grating normal and θ_i is measured counterclockwise from the normal.

E. THE ALL-REFLECTION MICHELSON INTERFEROMETER

The All-Reflection Michelson Interferometer (AMI) is a modified version of a conventional Michelson interferometer which utilizes a blazed diffraction grating vice a partially silvered mirror to split and to redirect the incident light rays. A schematic diagram of a conventional Michelson interferometer is shown in Figure 8.

As shown in the diagram, collimated light strikes a beam splitter positioned at angle of 45° to the incident radiation. The beam splitter separates the light into two rays, forcing the resultant plane waves to travel in different directions. One beam is reflected from a fixed mirror back to the splitter while the other beam is reflected off a movable mirror. The two rays are then recombined by the beam splitter and directed towards the detector. Adjusting the movable mirror will change the distance one of the beams travels, changing the interference pattern at the detector. If the path length difference between the two waves is zero or a multiple of the wavelength, constructive interference will occur. If the path length difference is a multiple of one half a wavelength, destructive interference will take place. Translating the movable mirror in one direction will cause the intensity at the detector to alternate from bright to dark.

It was not possible to use a conventional interferometer design for our objectives because the emissions of interest fall into the EUV and FUV portion of the electromagnetic spectrum, and most optical elements are opaque to light in this region. Several all-reflection

interferometers utilizing diffraction gratings as beam splitting devices have been built and evaluated (Roesler and Harlander, 1990; Fonck et al., 1978; Kruger et al., 1973).

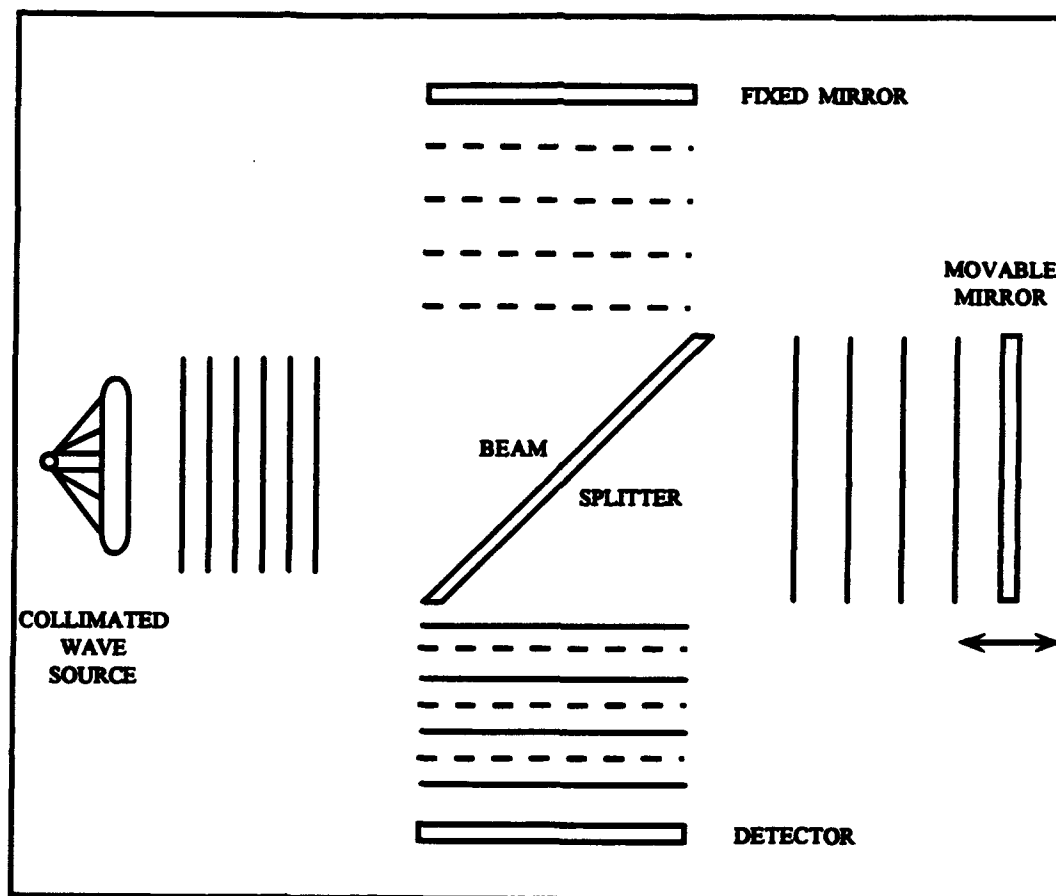


Figure 8 Michelson Interferometer

The prototype instrument examined in this thesis was first developed by Wallace (1992). The AMI is shown in Figure 9 and consists of a beam collimator, a plane diffraction grating, two plane mirrors and a detector. The collimator can contain a number of elements but is usually comprised of an aperture (pinhole or slit) and an off-axis parabolic mirror. The aperture is placed at the focus of the parabolic mirror so that light reflected from the mirror is collimated. In the diagram, the minus one order beam is represented by solid arrows and the zero order beam is shown as dotted arrows. The ray paths are also numbered to indicate the sequence of reflections

from when beams first hit the grating to when they recombine at the detector. Light striking the blazed grating is split along two separate paths corresponding to the zero and minus one diffraction orders. Plane mirrors are positioned to reflect the incident beams directly back to the diffraction grating. As a matter of convenience, the plane mirrors are designated by the diffraction order of the light they reflect back to the grating; the minus one order mirror reflects the minus one order beam and the zero order mirror the zero order beam. To ensure that the optical path lengths for both rays are equal, the zero order mirror is mounted on an adjustable base. The beams are again diffracted by the grating with the exception that the diffraction orders are reversed. In this way, the light recombines along a common path from the grating to the detector and creates an interference pattern.

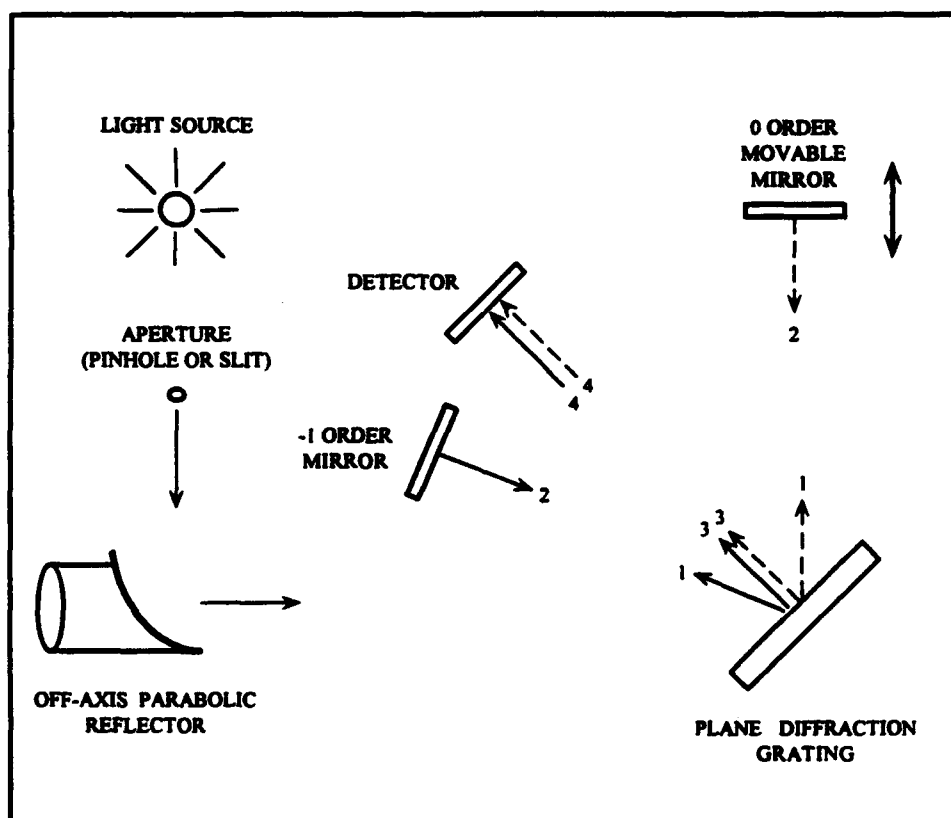


Figure 9 All-Reflection Michelson Interferometer

Recall from Equation (13) that the direction in which a wavefront propagates after striking the grating depends on the radiation wavelength (λ), the diffraction order (m) and the angle of incidence (θ_i). The dependence on wavelength, in particular, allows for unique characteristics and forms the basis of operation of the AMI. Figures 10, 11 and 12 illustrate the effects of wavelength and diffraction order on the plane waves, and the general operating principles of the AMI.

Figure 10 details the initial reflection of the plane waves from the diffraction grating. As in Figure (9), the minus one order plane waves are shown as solid lines while the zero order waves are pictured as dashed lines.

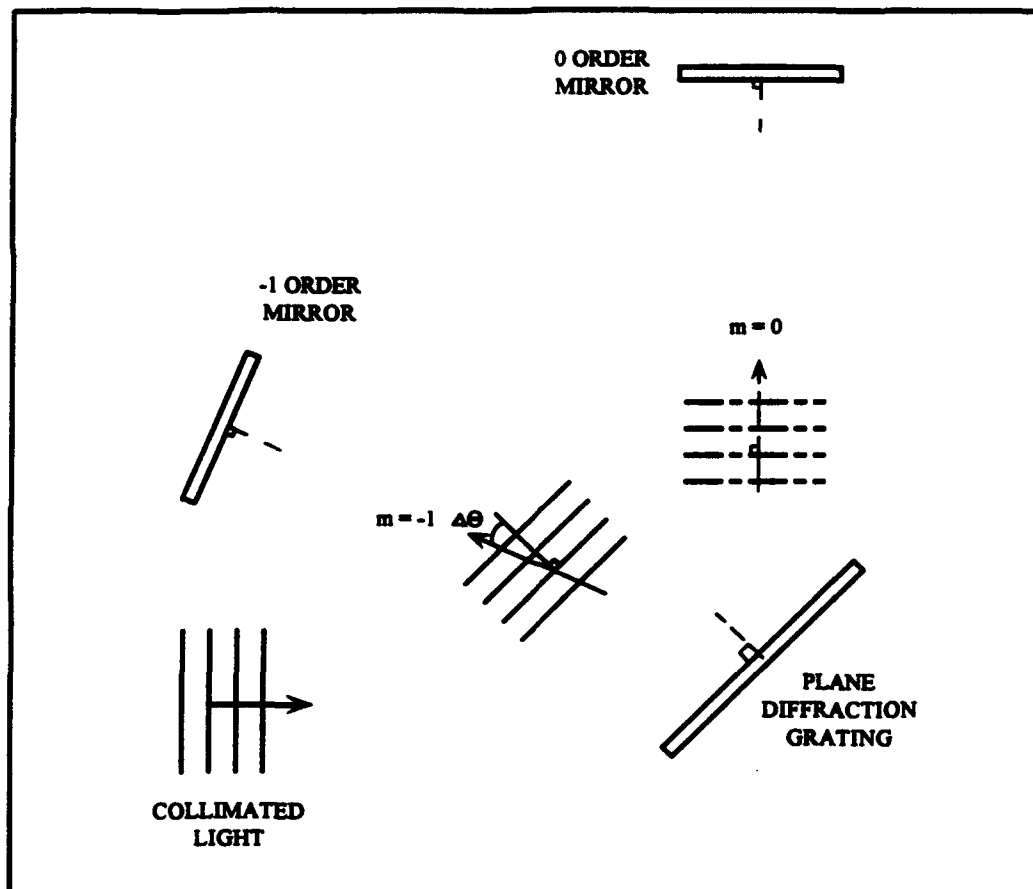


Figure 10 AMI - Reflection from Diffraction Grating

The zero order beam shows no angular dispersion because the angle of incidence equals the angle of reflection when $m=0$. The minus one order beam, on the other hand, experiences an angular shift of $\Delta\theta$ due to its diffraction order ($m=-1$) and λ .

Figure 11 shows the effect the plane mirrors have on the propagating wavefronts. The zero order beam approaches perpendicular to the mirror which means it is reflected perpendicular to the mirror. The minus one order beam travels toward the mirror with an angular dispersion of $\Delta\theta$; therefore, it reflects off the mirror with the same $\Delta\theta$. The mirror shifts the $\Delta\theta$ to the opposite side of the normal, but it does not add any additional angular shift.

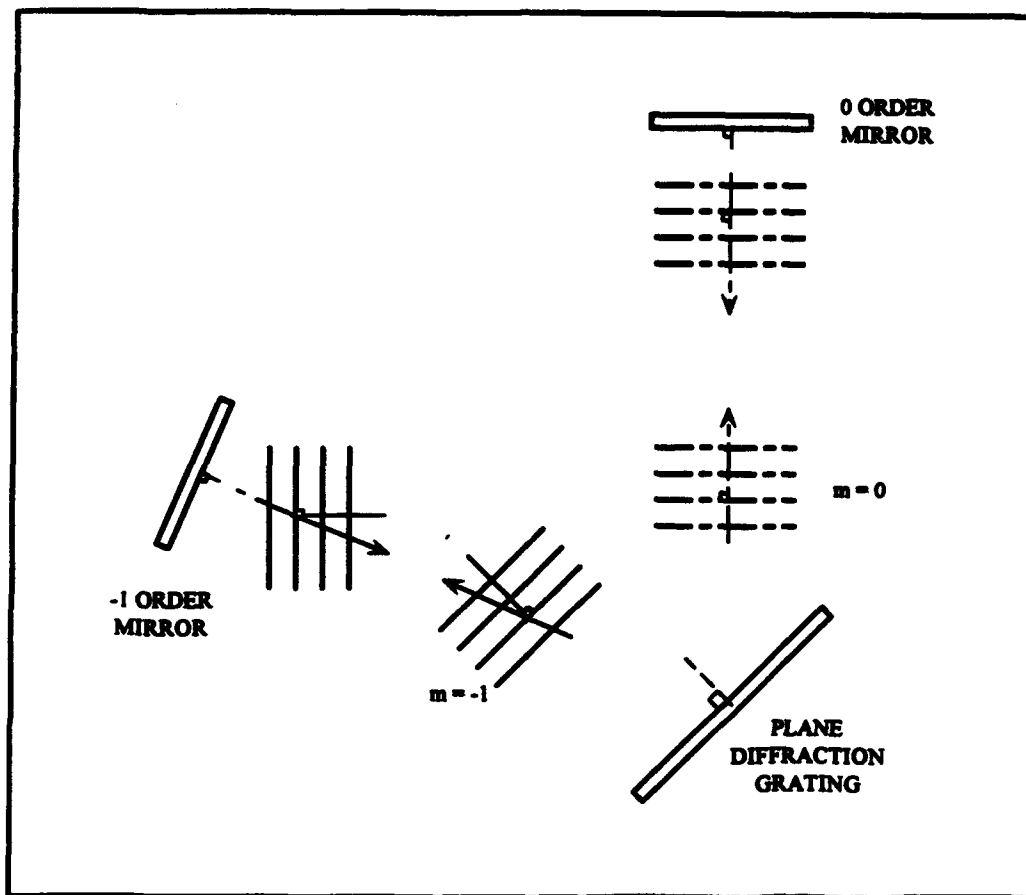


Figure 11 AMI - Reflection from Plane Mirrors

Figure 12 illustrates the second reflection of the beams from the grating and the recombination of the wavefronts at the detector. For the second reflection the diffraction orders are reversed. The minus one order beam undergoes an $m=0$ reflection while the zero order beam experiences an $m=-1$ reflection. This means that the zero order beam, not the minus one order beam, exhibits an angular shift of $\Delta\theta$ after reflecting from the grating.

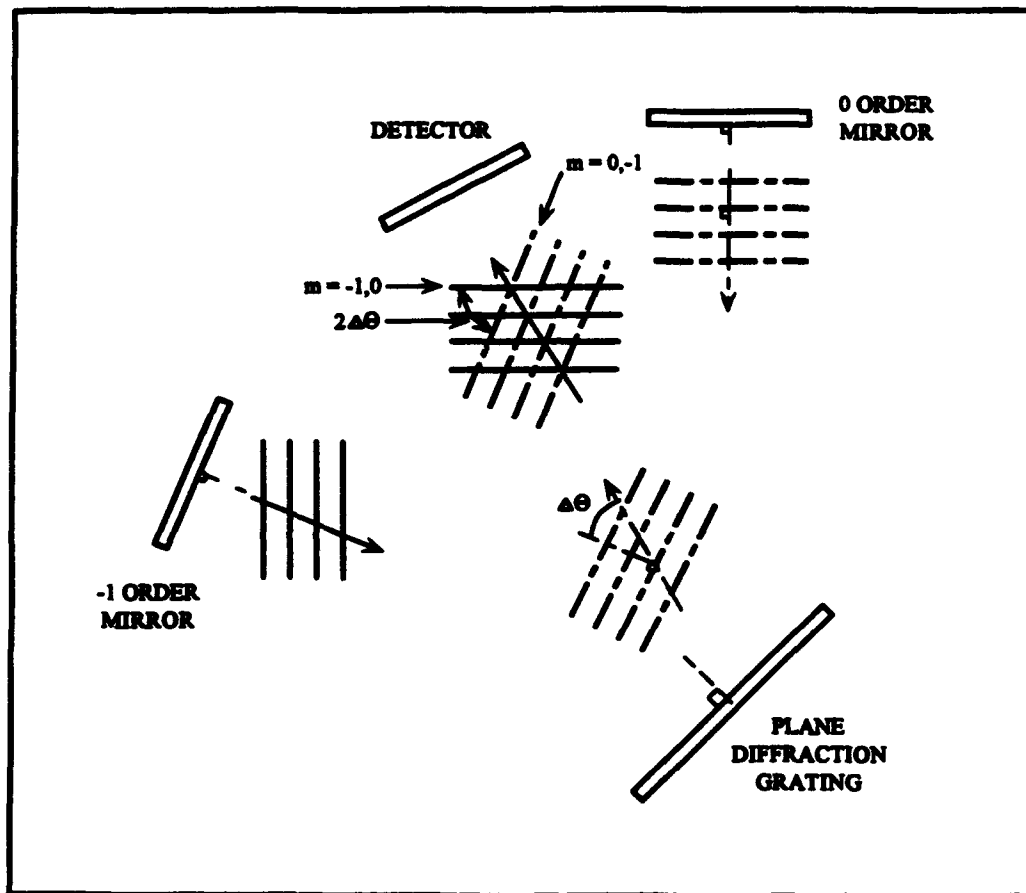


Figure 12 AMI - Recombination at Detector

As Figures 10, 11 and 12 show, each ray undergoes an angular shift of $\Delta\theta$ at some point along its optical path length. Each ray is shifted by the same amount, but in opposite directions, so that the total angular dispersion at the detector is $2\Delta\theta$ (where θ depends on λ). This is illustrated in Figure 12 and the enlarged view at the detector of Figure 13.

By adjusting the mirrors to exactly offset the angular shift of the wavefronts for a particular wavelength, λ_0 , the rays will arrive at the detector parallel to each other and interfere constructively at all points. In other words, the light at the detector will appear identical to the incident light. When the AMI is adjusted for a particular wavelength in this manner, the wavelength is referred to as the "tuned" wavelength (λ_0).

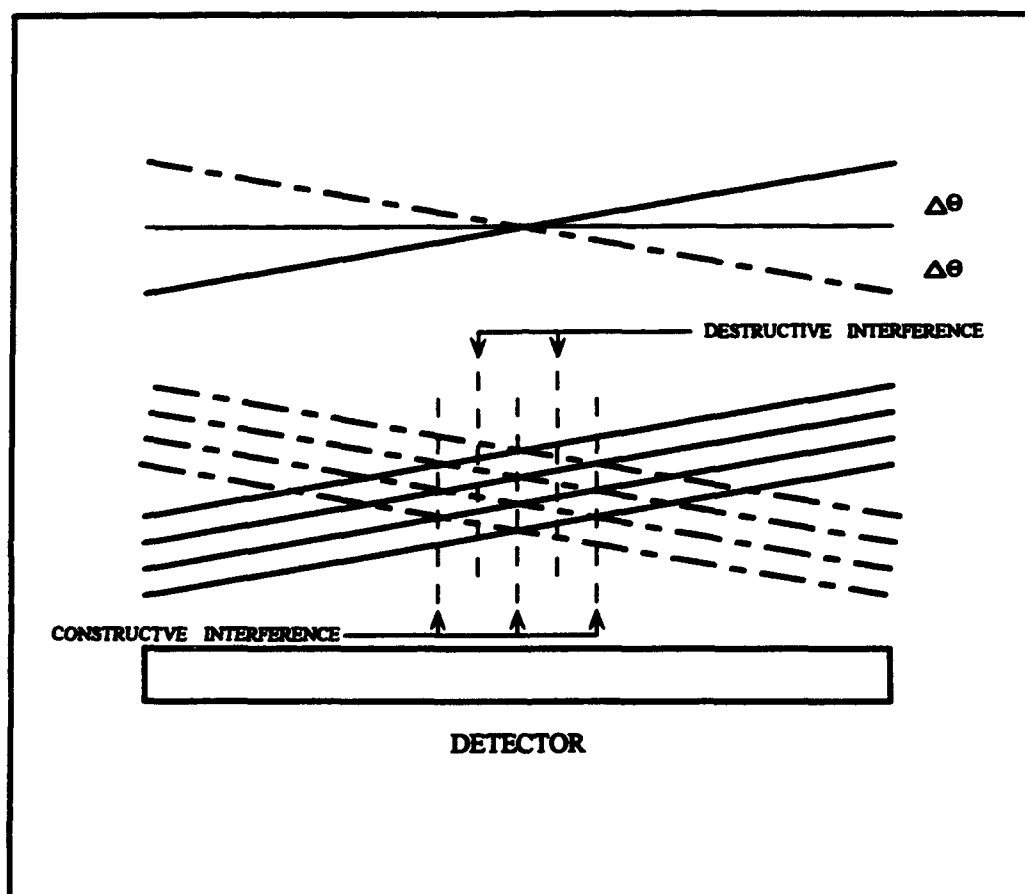


Figure 13 Expanded View of AMI at the Detector

Figure (14) represents a specialized case of Figure (13) where the mirrors of the AMI have been adjusted to produce one fringe cycle across the detector. The lowest spatial frequency occurs when one bright fringe and one dark fringe strike opposite ends of the detector with length L . The diagram of Figure (14) and Equation (13) can be used to calculate the resolution

limit of the AMI. For the first diffraction order ($m=1$), the "tuned" condition can be determined by setting the incident angle equal to the diffraction angle ($\theta_i = -\theta_m = \theta$). Equation (13) then becomes

$$\sin(\theta) = \frac{\lambda_0}{2a}, \quad (14)$$

and solving for θ gives

$$\theta = \sin^{-1}\left(\frac{\lambda_0}{2a}\right). \quad (15)$$

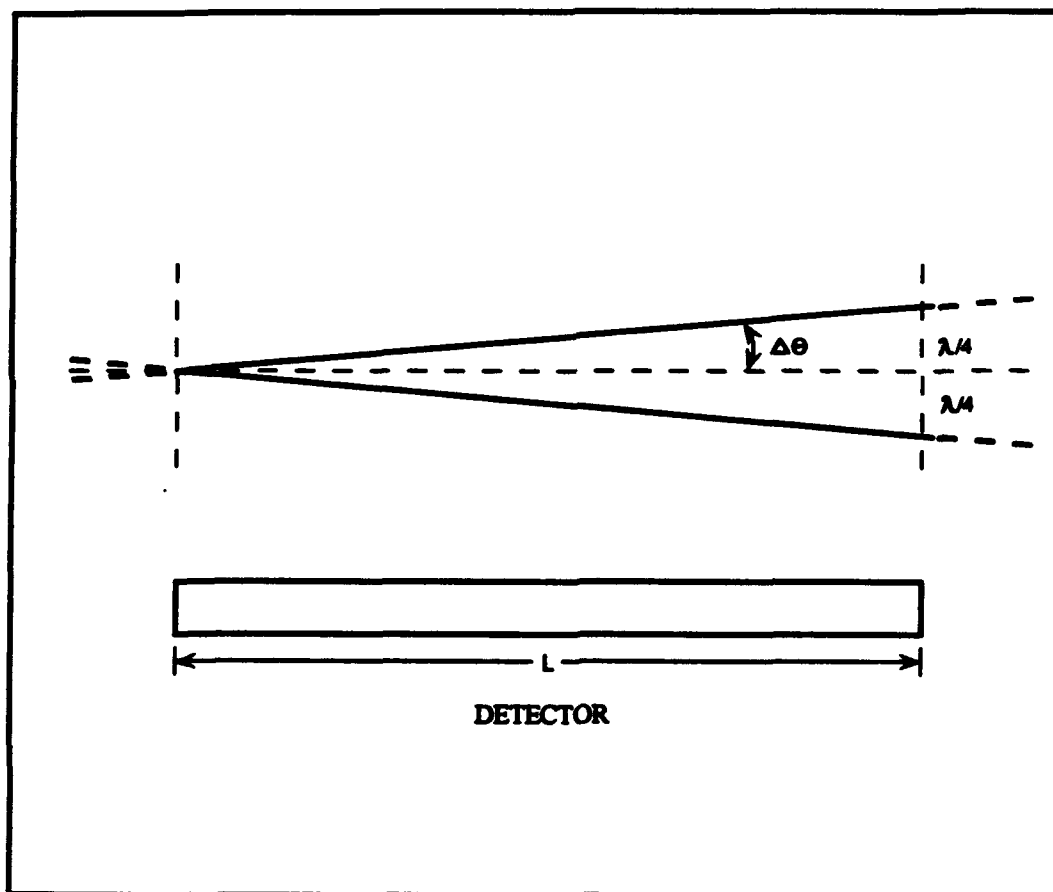


Figure 14 Minimum Resolution of the AMI

Once θ has been determined for the tuned condition, Equation (13) can be manipulated to determine the relationship between changes in wavelength and changes in angular dispersion. For small incremental changes, $\delta\theta$ can be approximated by $\Delta\theta$, and the derivative of Equation (13) becomes

$$\Delta\lambda = a \cos(\theta) \Delta\theta . \quad (16)$$

Performing a trigonometric identity substitution for the cosine term and replacing the resulting sine term with Equation (13) yields

$$\Delta\lambda = a\Delta\theta \sqrt{1 - \sin^2(\theta)} = a\Delta\theta \sqrt{1 - \left(\frac{\lambda_0}{2a}\right)^2} , \quad (17)$$

which is valid for any value of $\Delta\theta$.

Using the small angle approximation ($\tan(\Delta\theta) \approx \Delta\theta$), $\Delta\theta$ from Figure (14) can be expressed as

$$\Delta\theta = \frac{\lambda_0 / 4}{L} . \quad (18)$$

With this relationship between $\Delta\theta$, λ_0 and L , Equation (17) becomes

$$\Delta\lambda_{\min} = \frac{\lambda_0}{4L} \sqrt{a^2 - \left(\frac{\lambda_0}{2}\right)^2} , \quad (19)$$

where $\Delta\lambda_{\min}$ is the limit of resolution for the instrument. Using this method, Wallace (1992) calculated a typical resolution of the AMI to be approximately 4 mÅ.

For the AMI, which uses a blazed diffraction grating, Equation (13) can also be written as

$$\rho m \lambda = \sin\theta_m - \sin\theta_i , \quad (20)$$

with ρ representing the ruling density of the grating in lines/mm ($\rho=1/a$). Cleary et al. (1992) have shown that judicious selection of ρ with respect to λ will maximize the light incident on the detector by eliminating all reflections of unwanted diffraction orders. Using the conditions that θ_1 and all higher order diffraction orders are greater than 90° and θ_2 and all lower order diffraction orders are less than or equal -90° , Equation (20) can be solved for ρ to give

$$\rho_{\min} = \frac{2}{3\lambda}, \quad (21)$$

where ρ_{\min} is the minimum acceptable ruling density for the AMI. Using Equation (21), Wallace (1992) has shown that $\rho_{\min}=6000$ lines/mm is desirable for the oxygen 1304-Å emission lines.

F. THE SOLAR OXYGEN 1304-Å TRIPLET LINE PROFILES

The solar spectrum is dominated by strong emission lines below approximately 1500-Å. Although the strongest of these lines are attributed to atomic hydrogen and helium, there is also a strong atomic oxygen emission at 1304-Å. The brightness of this emission is due to the accidental resonance between the Lyman- β line of hydrogen at 1026-Å and a ground state transition of atomic oxygen. This resonance is known as the "Bowen mechanism" and it produces three oxygen emission lines at 1302.17, 1304.86 and 1306.02-Å. Since the solar atmosphere is extremely opaque at these wavelengths, all three lines display a pronounced self reversal at the center of the line profiles. The 1304.86-Å emission line was examined in this thesis, but the other two emission lines are similar and can be modeled in the same fashion.

The Doppler-broadened 1304.86-Å line profile can be approximated as the sum of two equal and offset Gaussian curves according to the equation

$$\pi F(x) = \frac{\pi F}{2\sqrt{\pi} x_{ds}} \left[e^{-\left(\frac{x-x_d}{x_{ds}}\right)^2} + e^{-\left(\frac{x+x_d}{x_{ds}}\right)^2} \right], \quad (22)$$

where $\pi F(x)$ is the flux in $\text{ergs cm}^{-2} \text{sec}^{-1}$, πF is the line-integrated flux in $\text{ergs cm}^{-2} \text{sec}^{-1}$, x_{dis} is a measure of the line dispersion in km/sec and x_{off} is a measure of the offset of the emission peaks from the center of the line in km/sec. This method was developed by Gladstone (1992) who generated an empirical fit to data obtained from the Solar Maximum Mission (SMM). Equation (22) is expressed in terms of flux and velocities. For the purposes of this thesis, it is more convenient to speak in terms of relative intensity and wavelengths. Expressed in these units, Equation (22) becomes

$$I_{\text{Solar}} = I_0 \left[e^{-\left(\frac{\lambda - \lambda_0 + \lambda_{\text{off}}}{\lambda_{\text{dis}}}\right)^2} + e^{-\left(\frac{\lambda - \lambda_0 - \lambda_{\text{off}}}{\lambda_{\text{dis}}}\right)^2} \right], \quad (23)$$

where I_0 is the maximum intensity and the offset and dispersion coefficients are as defined above (in units of Å). A model of the 1304.86-Å emission line using the values $\lambda_{\text{off}} = .0478\text{-Å}$ and $\lambda_{\text{dis}} = .0478\text{-Å}$ is shown in Figure 15. The Interactive Data Language (IDL) procedures used to generate the profile are listed in Appendix A.

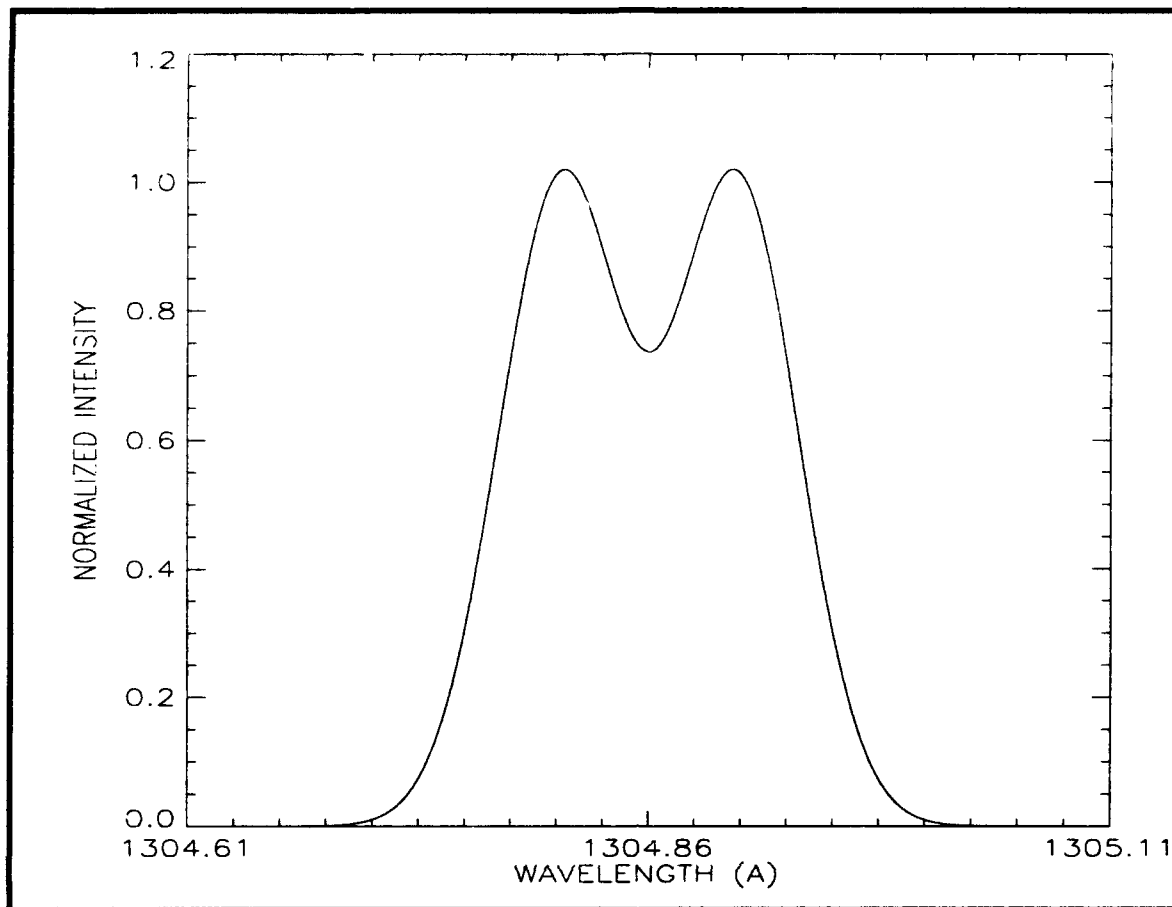


Figure 15 Solar Oxygen 1304.86-Å Emission Line Profile

G. THE TERRESTRIAL OXYGEN 1304-Å EMISSION

The oxygen 1304-Å triplet emission is also a prominent feature of the terrestrial airglow. The terrestrial emission is caused by solar resonant scattering and photoelectron impact excitation of atomic oxygen in the thermosphere. The terrestrial emission differs from the solar emission in that it displays a narrower lineshape and the intensity is much weaker (the solar emission is over 10^4 times as bright as the terrestrial emission).

The shape of the terrestrial oxygen 1304-Å line profile is dominated by two line broadening mechanisms, Doppler broadening and natural broadening. Of the two, Doppler

broadening is probably the easiest to understand. Atoms in a gas are always in random thermal motion, and the average speed of the atoms is dependent on the amount of thermal kinetic energy they possess. From the point of view of a stationary observer, this means that at any instant the atoms will be traveling at different velocities, some towards the observer and some away from the observer. As a result, the frequency of emission or absorption of each atom in its own frame corresponds to a different frequency from that for an observer. Each atom has its own Doppler shift which spreads the emission or absorption line out (although the total strength remains constant). The broadening of the line can be described by a simple Gaussian line profile. The relationship between temperature and the Doppler width of the spectral line is given by

$$\Delta\nu_{\text{Doppler}} = \frac{\nu_0}{c} \sqrt{\frac{2kT}{M}}, \quad (24)$$

where $\Delta\nu$ is the thermal Doppler width (in units of frequency), ν_0 is the line center frequency, c is the speed of light, k is Boltzmann's constant, T is the temperature and M is the atomic mass. In terms of Doppler wavelengths, Equation (24) becomes

$$\Delta\lambda_{\text{Doppler}} = \frac{\lambda_0}{c} \sqrt{\frac{2kT}{M}}. \quad (25)$$

The line-center cross section for each atom is

$$\sigma_{\nu_0} = \frac{\pi e^2}{mc} f_{12} \frac{1}{\Delta\nu_d \sqrt{\pi}}, \quad (26)$$

for the case of Doppler broadening. Replacing the constants of Equation (26) with numerical values gives

$$\sigma_{\nu_0} = 1.6 \times 10^{-14} \lambda_0 \sqrt{A/T} f_{12}, \quad (27)$$

with λ_0 in Å and T in K. A is the atomic weight of the atom and f_{12} is the oscillator strength. Oscillator strength is defined as the ratio of the radiative decay rate of a real atomic transition to the decay rate of a classical electron oscillator at the same frequency. Since it is a ratio of rates, the oscillator strength is dimensionless.

Natural broadening is a result of the Heisenberg uncertainty principle which relates the energy and lifetime of a system. In equation form the uncertainty principle is

$$\Delta E \Delta t \geq \hbar / 2, \quad (28)$$

where ΔE is the uncertainty in the energy of the system, Δt is the time interval characteristic of the rate of change of the system and $\hbar = h/2\pi$. If the lifetime of an atomic state is long (approx. 10^{-3} sec) then the line profile will be relatively narrow, whereas atomic states that are short-lived (approx. 10^{-8} sec) display broad lineshapes. For natural broadening, the widening of the spectral line can be described by a Lorentzian line profile.

Quite often, as in the case of the terrestrial 1304-Å emission, atoms exhibit both natural and Doppler line broadening effects. In these situations, the lineshape can be described by the Voigt function, which is a convolution of the Lorentz profile over the Doppler profile. The terrestrial 1304.86-Å emission line profile can then be expressed as

$$I_{\text{Terrestrial}} = I_0 (\Delta \nu_D)^{-1} \pi^{-1/2} H(a, u), \quad (29)$$

where $H(a, u)$ is the Voigt function, and the Voigt parameters are defined as

$$a \equiv \frac{\Gamma}{4\pi\Delta\nu_D}, \quad (30)$$

$$u \equiv \frac{\nu - \nu_0}{\Delta\nu_D}, \quad (31)$$

$$\Gamma = \gamma_n + \gamma_l + 2\nu_{col}. \quad (32)$$

The parameters γ_u and γ_l are the widths of the upper and lower states involved in the transition and ν_{col} is the collision frequency.

A more detailed explanation of the Voigt function, and line broadening mechanisms in general, can be found in Rybicki and Lightman (1979). Figure (16) shows a comparison of Doppler and Voigt profiles for the terrestrial oxygen 1304.86-Å emission line. The IDL procedures used to model the profiles are listed in Appendix A. The terrestrial lines were generated using a temperature of 300 K and a Voigt parameter of $a=1.108 \times 10^{-2}$. As the diagram shows, the shape of the profiles are very similar near the center, but the Voigt curve widens out significantly near the edges while the Doppler profile remains fairly narrow. This indicates that Doppler broadening dominates near the center of the line profile while natural broadening and the Lorentzian lineshape is predominate in the regions away from line center.

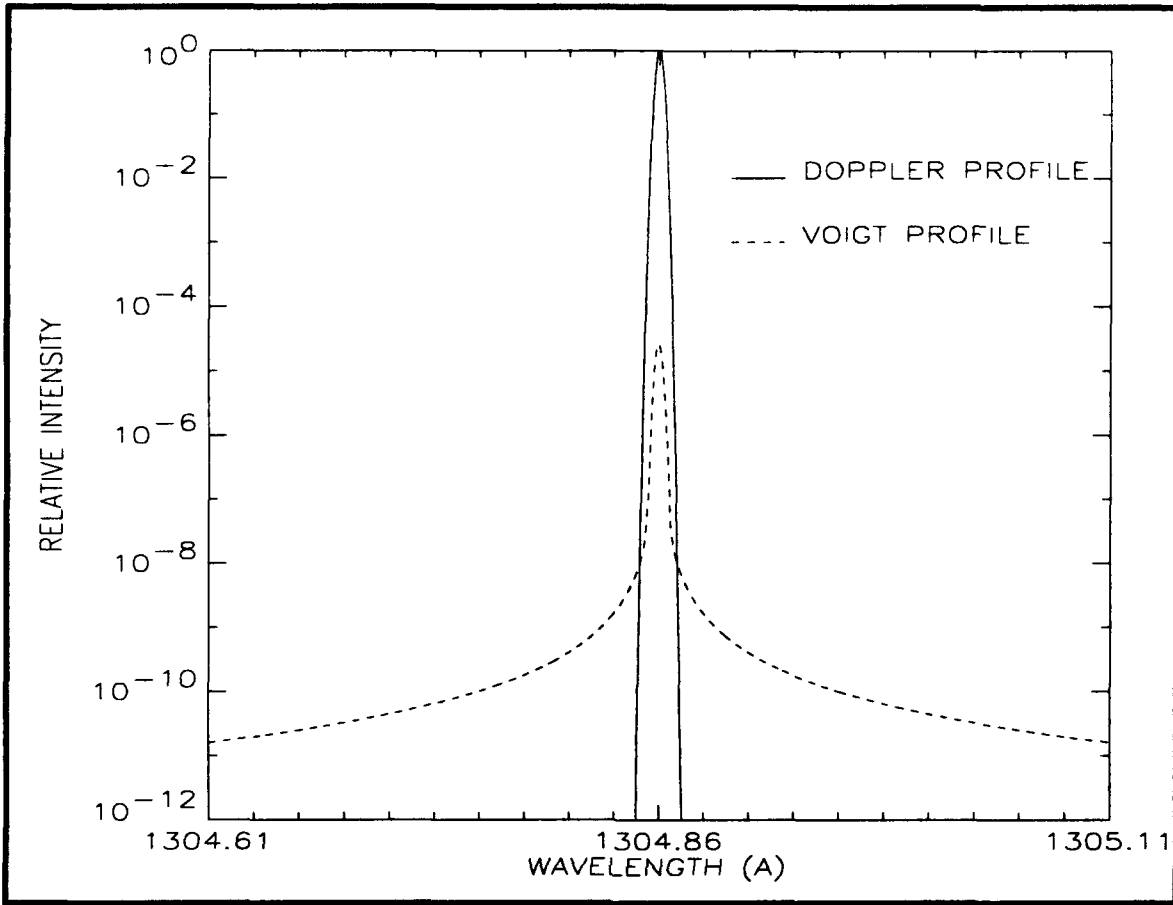


Figure 16 Comparison of Doppler and Voigt Line Profiles

H. SOLAR OCCULTATION

Observations of the solar oxygen 1304.86-Å emission line from within the atmosphere will be attenuated to some degree by the intervening column of oxygen, and the amount of absorption is directly proportional to the column density. The larger the column of oxygen between the observer and the solar emission, the greater the attenuation of the solar line. The equation describing the resulting lineshape is given by

$$I_{\text{Observed}}(\lambda) = I_{\text{Solar}}(\lambda)e^{-[N_o(\lambda)]}, \quad (33)$$

where N is the column density (cm^{-2}) and $\sigma(\lambda)$, the resonant scattering cross-section (cm^2), is given by

$$\sigma(\lambda) = \sigma_0 \Delta\nu_D H(a, u). \quad (34)$$

Since σ is also dependent on temperature, there are really two geophysical variables in Equation (33), N and T . Figures (17) and (18) show calculations of the variation of I_{Observed} with changing column densities. These calculations assumed an isothermal atmospheric temperature of 300 K and a Voigt parameter a of 1.108×10^{-2} . Figure (17) plots four curves, the unattenuated solar line profile and three other curves corresponding to column densities of 1×10^{17} , 1×10^{18} and $1 \times 10^{19} \text{ cm}^{-2}$. Since these column densities are representative of the actual column densities in the atmosphere, Figure (17) is a fairly accurate simulation of observed oxygen 1304.86-Å emission line profiles.

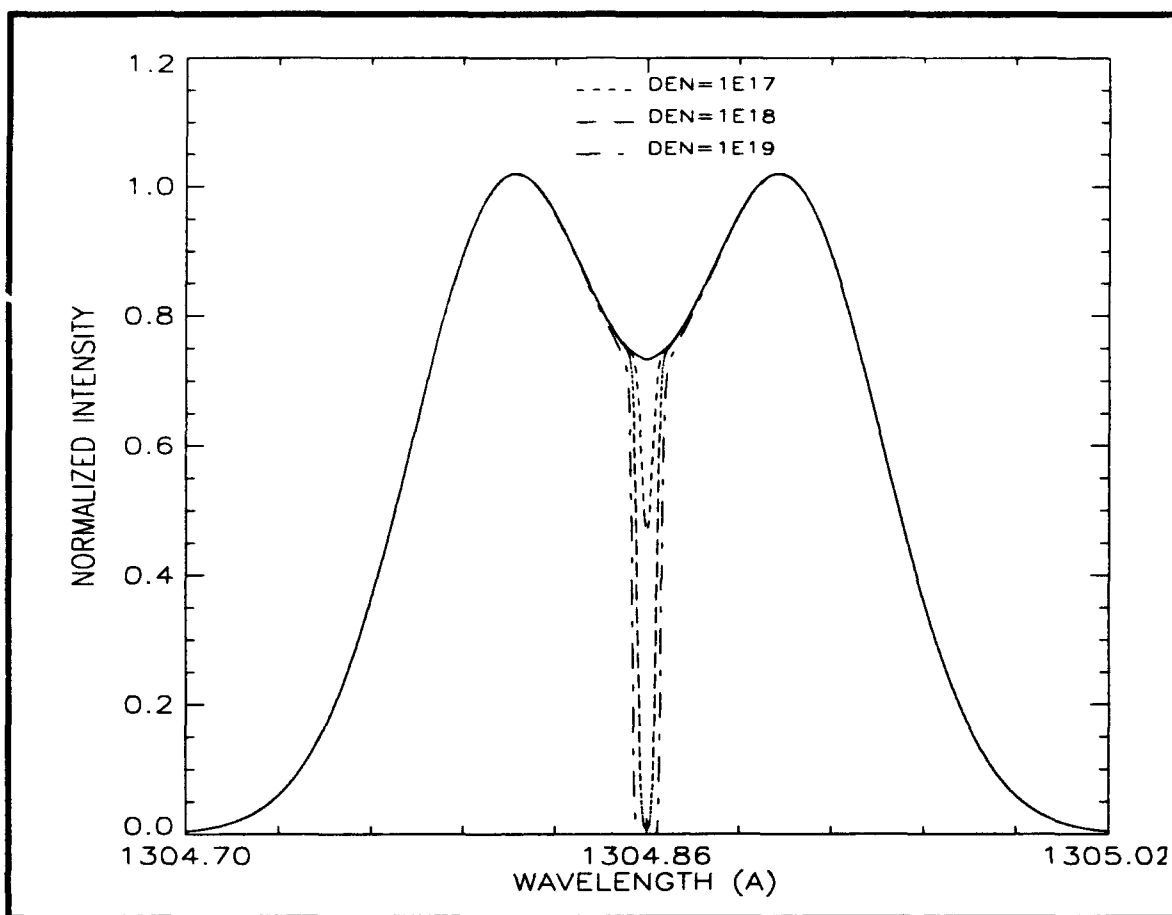


Figure 17 Simulated Oxygen 1304.86-Å Line Profile versus Column Density
($N=1 \times 10^{17}$, 1×10^{18} and 1×10^{19})

Figure (18) plots the simulated line profile for column densities of 1×10^{21} , 1×10^{22} and $1 \times 10^{23} \text{ cm}^{-2}$ and shows that at high column densities, the solar 1304.86-Å is almost completely attenuated by the atmosphere. These figures also indicate that any measurement technique of the observed oxygen 1304.86-Å line profile will be sensitive to the column of oxygen over the entire altitude range of the thermosphere. The IDL procedure used to model the observed intensity is shown in Appendix A.

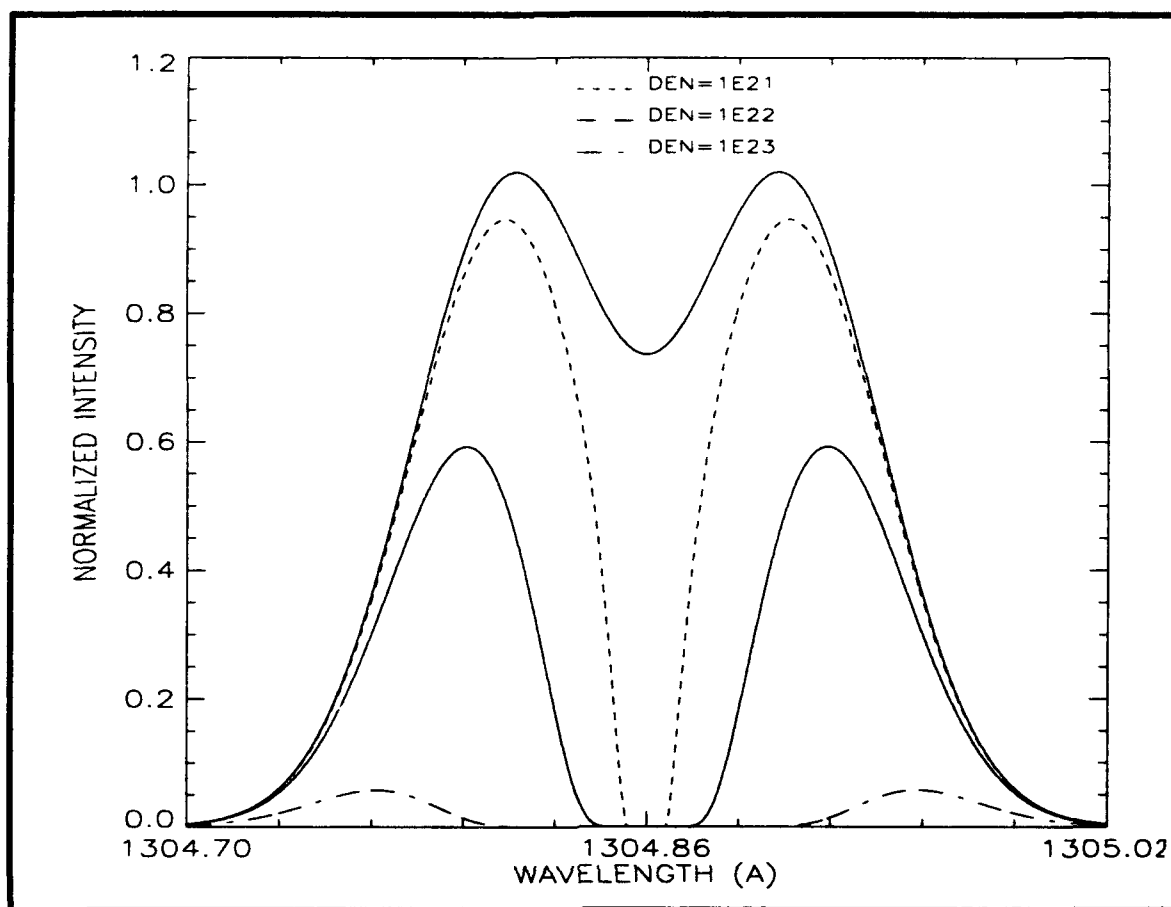


Figure 18 Simulated Oxygen 1304.86-Å Line Profile versus Column Density
($N=1 \times 10^{21}$, 1×10^{22} and 1×10^{23})

The profiles of Figure (19) illustrate the expected temperature dependence of an occultation measurement. The solid lines of Figure (19) depict the column densities of Figure (17) for a temperature of 300 K while the dashed lines plot the same column densities for a temperature of 1000 K.

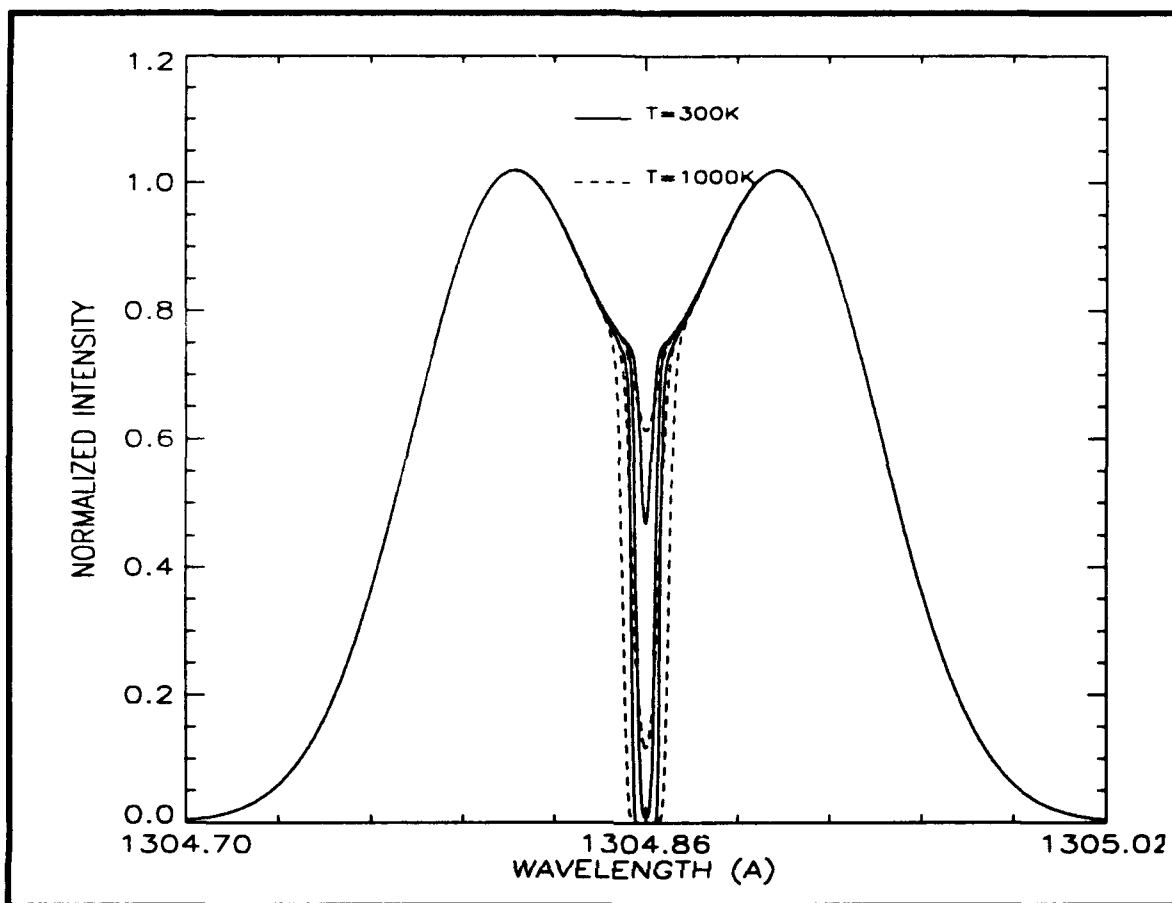


Figure 19 Simulated 1304.86-Å Line Profile versus Temperature

Figure (20) represents an enlarged view of Figure (19) around the center wavelength. Figures (19) and (20) show that higher temperatures broaden the absorption of the simulated line profile around the center at the same time as decreasing the depth of the attenuation. Although the total amount of attenuation remains fairly constant, the shape of the line profile is definitely affected by the temperature and must be accounted for when analyzing the lineshapes.

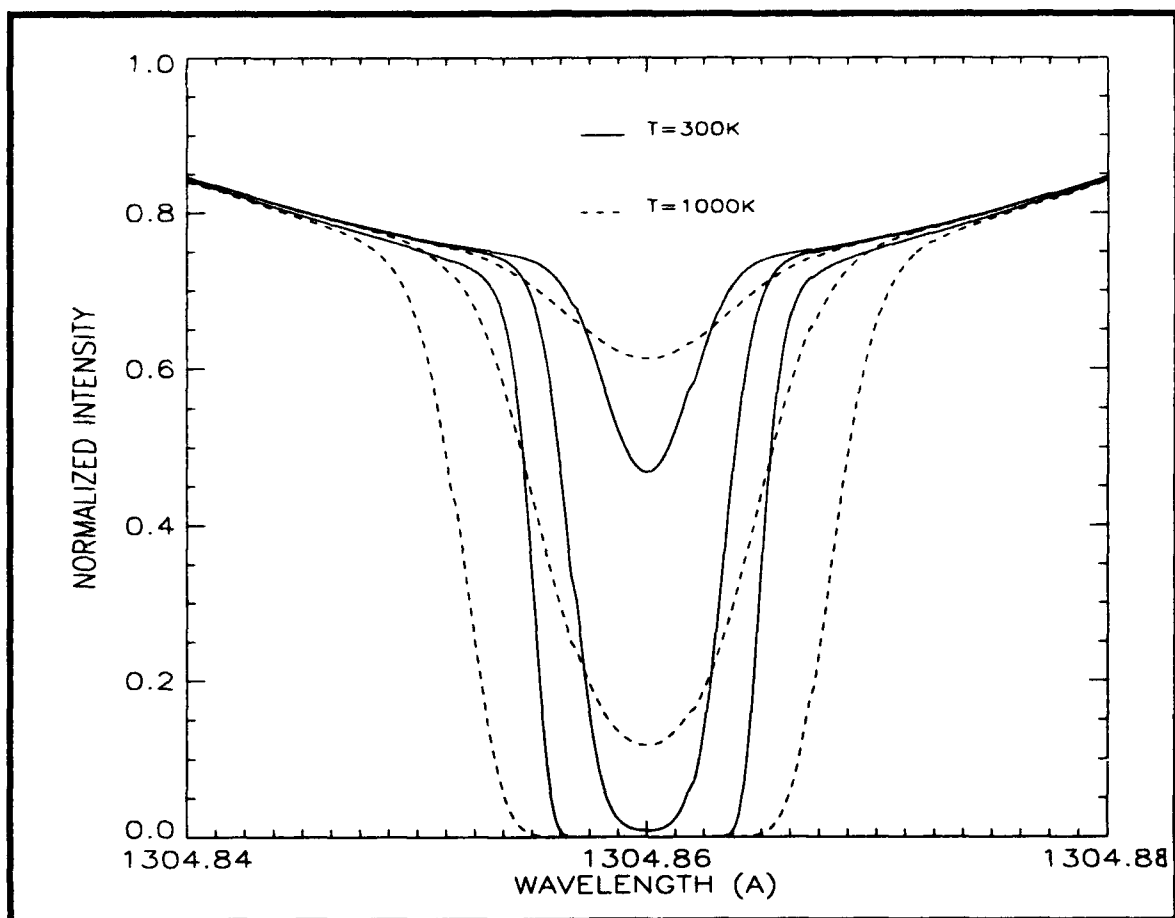


Figure 20 Enlarged View of Line Profile versus Temperature

Figure (21) is an illustration of the curve of growth for the total simulated oxygen 1304.86-Å emission at a variety of temperatures. The IDL procedure used to plot the growth curve is listed in Appendix A.

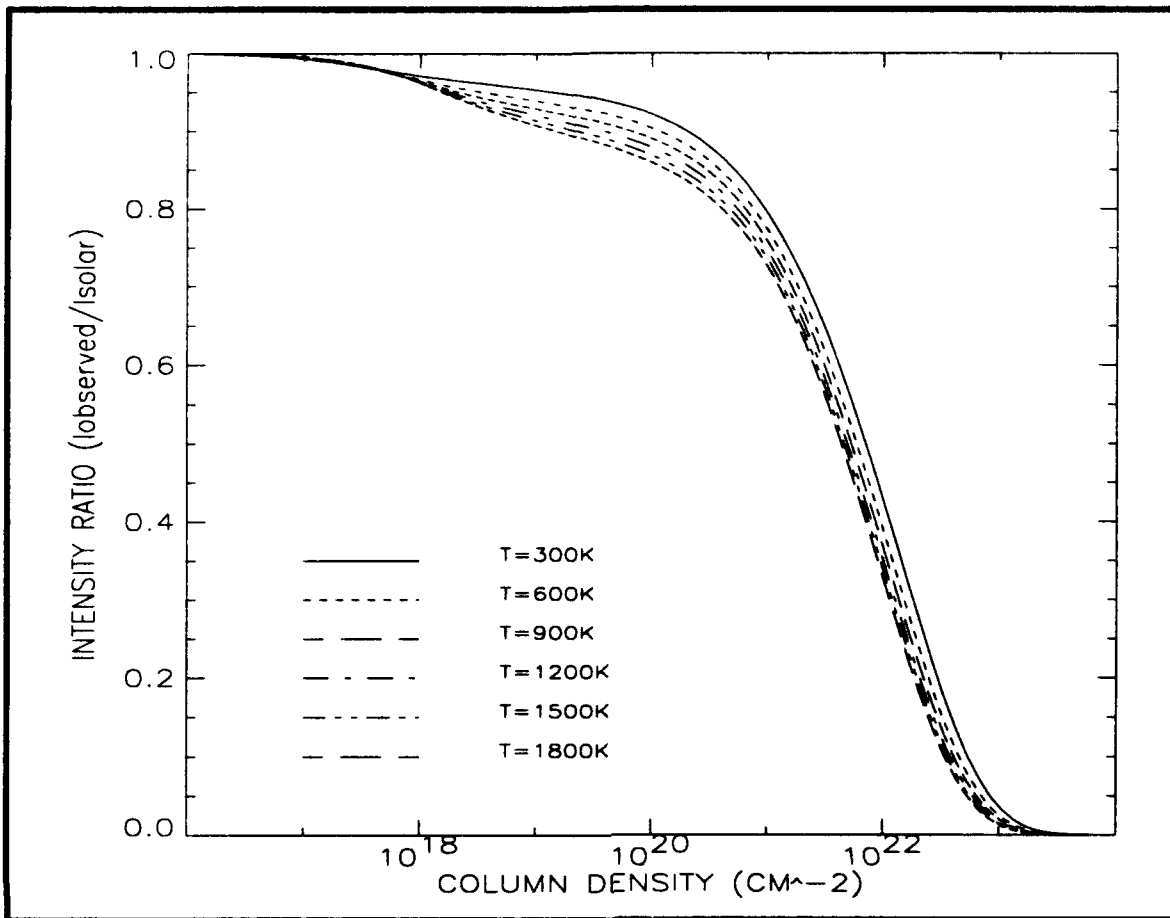


Figure 21 Growth Curve for Oxygen 1304.86-Å Line

Simulations of AMI performance by Carlson (1992) using the Dart ray tracing program show that AMI is an excellent instrument for observing the oxygen 1304.86-Å emission line. Once the line profile and temperature at various altitudes have been measured, the amount of atomic oxygen in the thermosphere can be determined using methods such as that developed by Meier (1992), which utilizes Discrete Inverse Theory to retrieve the oxygen concentration from solar occultation data.

IV. EXPERIMENT

This section describes the experimental procedures used to setup and test the prototype All-Reflection Michelson Interferometer.

A. SETUP OF AMI

The initial setup and testing of a prototype AMI was done by Risley (1992). He built an instrument similar to that described in Figure (9), with the exception that he inserted a lens between the light source and pinhole aperture in order to focus as much light as possible on the pinhole opening. After construction was complete, he proceeded to test the instrument using a number of different light sources. Unfortunately, he achieved only limited success due, primarily, to an inadequate detector. For a more detailed treatment of the original construction and prototype testing see Risley (1992).

The first step in the continuation of prototype testing was to increase the intensity of light reaching the detector. This was done by comparing the original grating ($\rho=1200$ lines/mm) to a sinusoidal diffraction grating with a ruling density of 2400 lines/mm. It was hoped that a sinusoidal grating with a higher ruling density would increase the intensity of light in the zero and minus one order beams. Measurements of beam intensity were made with both gratings using two different light sources, a He-Ne laser and a mercury vapor lamp. Figure 22 illustrates how the beams were designated and where readings were taken. Tables 1 and 2 are a compilation of the results. Table 1 shows the measurements in terms of light intensity (watts) while Table 2 depicts the results in terms of percentages. The $m=(0,-1)$ and $m=(-1,0)$ percentages of Table 2 are based on the intensities from the $m=0$ and $m=-1$ beam, not the initial beam. For example, the

$m=(0,-1)$ figure of 19.3 % for the He-Ne laser with the 1200 lines/mm grating was obtained by dividing 0.58 ($m=(0,-1)$) by 3.00 ($m=0$).

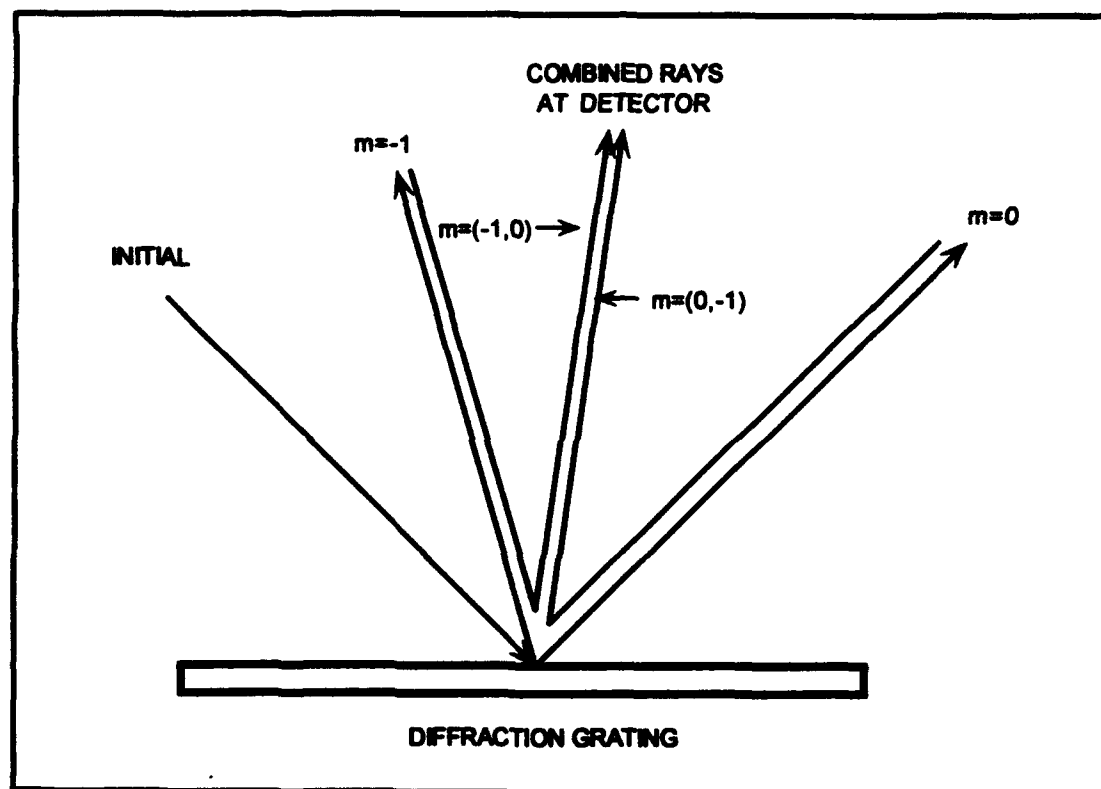


Figure 22 Diffraction Grating Comparison Diagram

TABLE 1 COMPARISON OF DIFFRACTION GRATINGS
(Standard with $\rho=1200$, Sinusoid with $\rho=2400$)

Reflection	He-Ne Laser (μW)		Mercury Lamp (nW)	
	1200	2400	1200	2400
Initial	19.6	16.7	30.5	33.2
$m=0$	3.00	11.6	6.40	23.5
$m=-1$	13.2	2.80	10.8	3.06
$m=(0,-1)$	0.58	1.52	0.60	1.50
$m=(-1,0)$	0.76	1.60	0.75	1.65
Combined	1.32	3.17	1.35	3.20

TABLE 2 PERCENTAGE COMPARISON OF GRATINGS
(Standard with $\rho=1200$, Sinusoid with $\rho=2400$)

Reflection	He-Ne Laser (%)		Mercury Lamp (%)	
	1200	2400	1200	2400
Initial				
m=0	15.2	69.5	21.0	70.8
m=-1	66.7	16.8	35.4	9.2
m=(0,-1)	19.3	13.1	9.4	6.4
m=(-1,0)	5.7	57.1	6.9	53.4
Combined	6.7	19.0	4.4	9.6

The results show that the sinusoidal grating achieved better results for both light sources than the standard grating. In fact, the sinusoidal grating showed a twofold increase in the light reaching the detector. The light intensity for the He-Ne laser went from 6.7% to 19.0% while the intensity for the mercury lamp went from 4.4% to 9.6%. Interestingly enough, the sinusoid grating distributed the light differently between the two diffraction orders. The sinusoidal grating sent more of the light to the zero order reflection while the standard grating sent the majority of light to the minus one order.

The next improvement made was to mount the optical workbench on a vibration isolation base. The Micro-g Series 62 post isolation system consisted of four supports bolted together with tiebars to comprise a structurally sound rectangular base. Each support contained an air piston and leveling valve for final adjustments. A pressurized nitrogen gas tank provided air to the pistons and main pressure was maintained at approximately 60 psi with a regulating valve.

The third refinement, shown in Figure 9, was to mount the zero order mirror on an adjustable base to insure the path lengths for both rays were equal (within the coherence length of the light source).

The final, and perhaps most important, modification to the original prototype was to replace the Panasonic CCD video camera with a solid state Electrim EDC-1000HR integrating CCD camera. The EDC-1000HR consisted of a camera head assembly, a computer interface card and connecting cable and was controlled directly from the computer keyboard. The sensing area of the detector was 8.67 mm wide by 6.59 mm high and the pixel array (resolution) was 753 horizontally by 244 vertically. One of the main advantages of the EDC-1000HR camera was that images on the computer screen could be saved directly to hard drive or floppy disk as TIFF files for later manipulation and analysis. Other important features included the ability to control exposure time from 1 msec to 1 minute and to subtract background light from the picture.

B. TESTING WITH MERCURY VAPOR LAMP

The first step in testing the interferometer design was to create an interference pattern using a light source with a short coherence length. A low pressure mercury discharge tube mounted in an Oriel model 65160 lamp, such as that used by Risley (1992), was chosen. A band-pass filter was placed across the opening of the lamp to filter out all emission lines from the discharge tube except the green line of interest at a wavelength of 5461-Å.

The setup was exactly the same as Risley's (1992). A convex lens was placed between the lamp and a 250 μm pinhole and the pinhole was placed at the focus of the lens to maximize the light throughput. The Oriel Model 45347 off-axis parabolic mirror was focused as before, using a small telescope focused at infinity. Since the sinusoidal diffraction grating increased the light intensity of the beams, the zero and minus one order mirrors were aligned by observing the reflections from the grating and placing the mirrors visually in the beams so that the light bounced off the mirrors and returned to the same spot on the diffraction grating.

Once the initial setup and alignment was complete, the computer camera was turned on and actual testing commenced. It took only a few minutes to adjust the mirrors and establish an interference pattern. Figure 23 is a picture of the first interference pattern achieved with the mercury vapor lamp at 5461-Å.

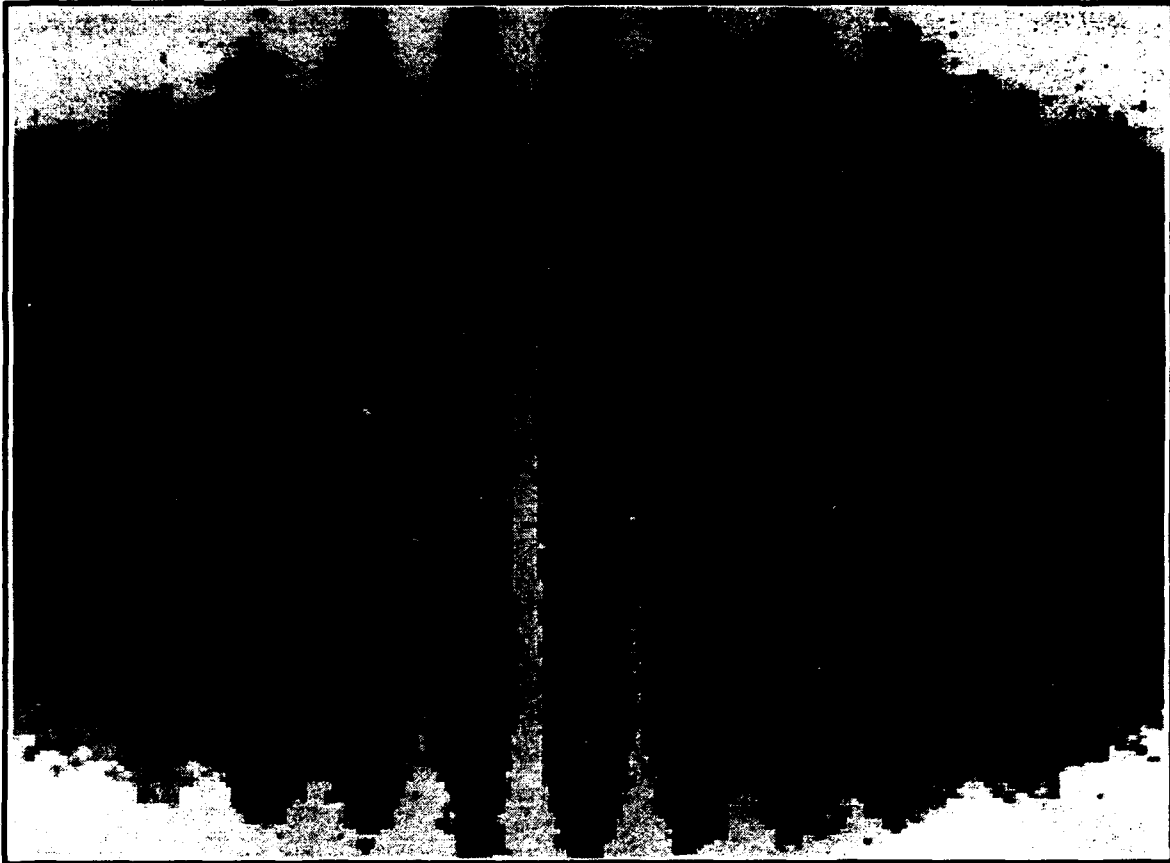


Figure 23 Initial Interference Pattern for Mercury Vapor Lamp

The exposure time for the interference pattern was 1 sec and the image was recorded using the HWINCAM software provided with the computer camera. The HWINCAM program only provided a pixel resolution of 192 (H) \times 180 (V) and was used only for the first picture. All subsequent images were recorded using the HVESA program (also supplied by Electrim) which provided the maximum resolution of 753 (H) \times 244 (V).

Once the pattern was established, fine adjustments to the system were made to improve the contrast and center the pattern. The minus one order mirror had two adjustment screws, one to control the vertical angle and another the horizontal angle of the mirror. Adjusting the vertical screw affected the tilt of the interference lines. If the screw was turned far enough in one direction, the fringes rotated a full 360 degrees. The adjustment screw was extremely sensitive and it proved difficult to get the lines perfectly vertical. The horizontal screw controlled the spatial frequency of the interference pattern. Rotating the screw clockwise or counterclockwise moved the mirror angle closer to, or farther away from, the tuned wavelength and affected the number of interference fringes on the screen. As the wavelength approached λ_0 the number of fringes on the screen decreased. Moving the wavelength away from λ_0 had the opposite effect and increasing the mirror angle such that the wavelength was too far from λ_0 caused the fringes to disappear altogether.

Another important adjustment was the position of the zero order mirror from the grating. When the pattern was first established, the brightest fringes were near the right edge of the screen. Moving the mirror closer to the grating caused the bright fringes to move towards the center of the screen. When the distance from the zero order mirror to the diffraction grating equaled the distance from the minus one order mirror to the grating, the brightest fringes were in the center of the screen and the interference pattern displayed the greatest definition.

Experimentation with screw adjustments and settings showed that the AMI was also very sensitive to vibrations and air currents around the mirrors. Even with the workbench resting on a cushion of air, footsteps or movement around the table caused the pattern on the screen to oscillate. The only way to create a stable pattern was to make adjustments and then stop all motion for a few minutes to give the interference pattern on the screen time to settle.

Since the AMI was working as predicted, all that remained was to record and analyze data for a number of sources. Three IDL procedures were written to analyze data recorded by the camera. The first procedure, named IMAGE, read information from an interference pattern (stored as a TIFF file from the EDC HVESA program) and displayed the image on the screen. The second procedure, called PROFILE, vertically summed the intensities of bright and dark fringes from the interference pattern. The net result was an interference profile (753x1 array) which showed the variation of light intensity as a function of fringe location on the detector. The final procedure, designated as SPECTRUM, took the Fourier transform of the interference profile to recover the initial spectrum. For the mercury emission at a wavelength of 5461-Å, which approximates a monochromatic light source, the resulting spectrum was a single spike some distance from λ_0 . A number of runs were conducted at different distances from the tuned wavelength and the following figures are indicative of the data collected. Figure 24 shows an interference pattern, Figure 25 an interference profile and Figure 26 the Fourier transform of the interference profile.

The image of Figure 24 is very similar to that of Figure 23. Close inspection of both figures reveals a background pattern that resembles a fingerprint. Every possible step was taken in an effort to localize the source of the background pattern. First, each light beam was blocked separately to see if one of the optical elements was responsible for the pattern. It made no difference which beam was blocked, as long as any light reached the detector the background pattern was visible. All elements common to both beams were also inspected to no avail. Finally, the detector was disassembled and the glass covering the solid state surface was cleaned in an effort to remove the pattern. Unfortunately, the glass was permanently affixed to the detector surface which prevented the surface itself from being cleaned. Eliminating all other sources for

the background pattern, it was surmised that the pattern was, indeed, an actual fingerprint which was deposited on the surface sometime during the manufacturing process.



Figure 24 Interference Pattern for Mercury Vapor Lamp

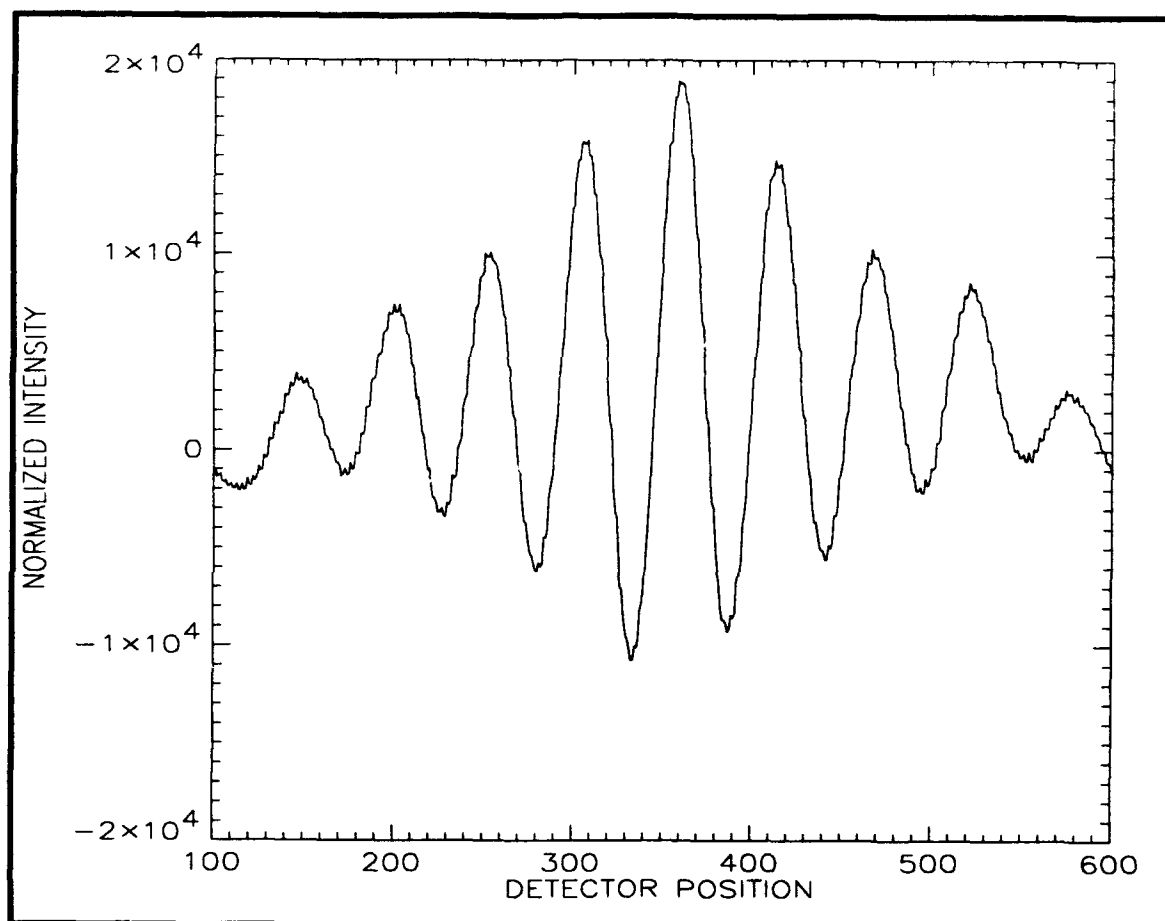


Figure 25 AMI Interference Profile for Mercury Vapor Lamp

The interference profile of Figure 25 is an excellent example of Fraunhofer diffraction. As expected, the number of peaks and valleys match the number of bright and dark fringes from Figure 24. Since the AMI measures wavelength relative to a particular tuned wavelength, the Fourier transform of the interference profile should produce a single peak at a position on the x-axis dependent on the number of bright fringes in the profile (number of fringes is a measure of spatial frequency). There are nine bright fringes in Figure 25 plus three or four not shown on the graph. Therefore, Figure 26 should display a single spike approximately 12 to 13 units from λ_0

(the zero point on the x-axis). Examination of Figure 26 reveals that it does indeed show a pronounced spike at that position.

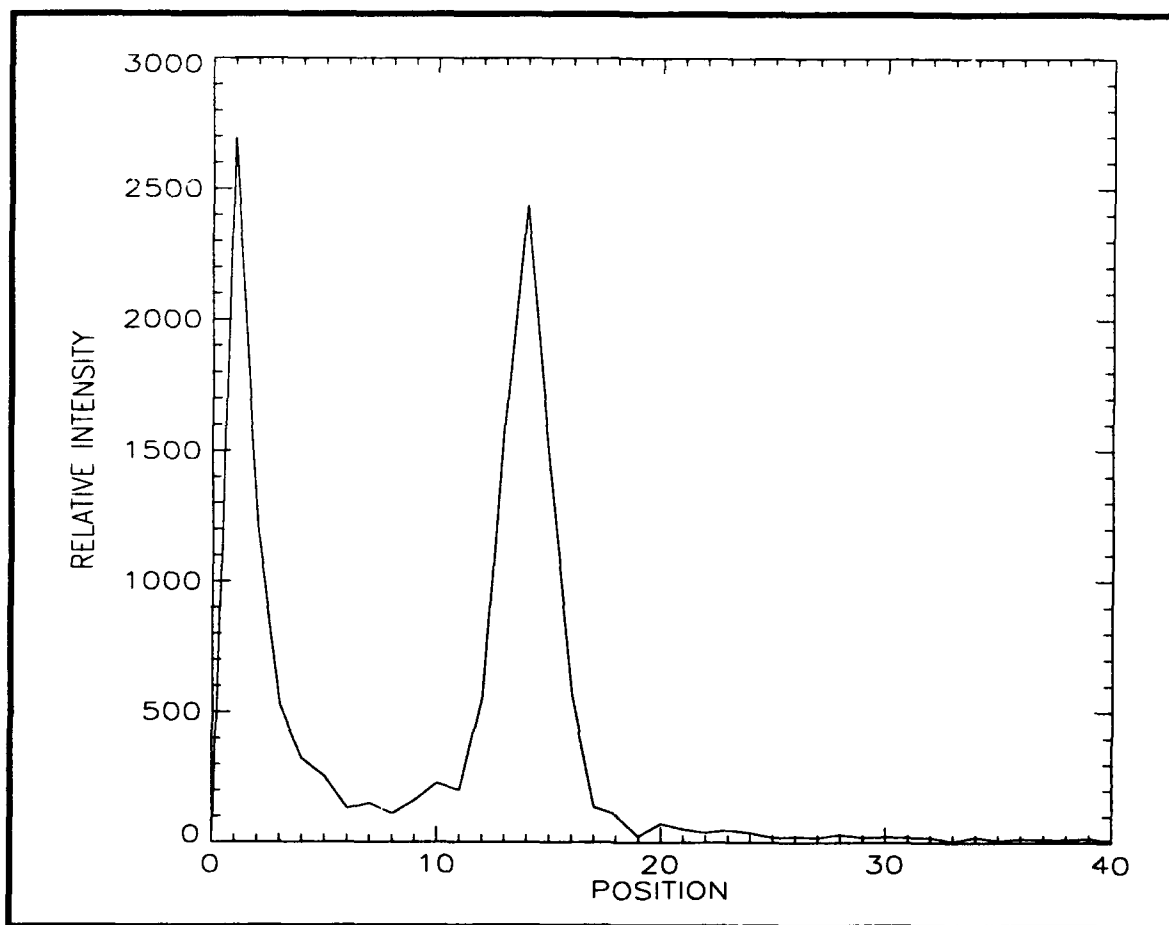


Figure 26 Fourier Transform for Mercury Vapor Lamp

The large peak near the origin of Figure 26 represents the low frequency noise component of the signal. This peak was present in all of the spectrums recorded during the experiment. In order to distinguish the actual wavelength peak from the background noise, it was necessary to adjust the AMI so that the interference pattern consisted of at least four or five bright fringes. This had the effect of moving the peak away from the low frequency noise.

Figures 27, 28 and 29 were recorded using the same monochromatic light source but at a higher spatial frequency than Figures 24, 25 and 26. The image of Figure 27 appears much cleaner and more defined than the image of Figure 24 because the background was subtracted from the interference pattern using the remainder feature of the EDC HVESA software.



Figure 27 Interference Pattern for Mercury Vapor Lamp (High Spatial Frequency)

Figure 28 shows 14 bright fringes, which means that, including the three or four fringes not shown, there should be a spike at approximately 17 or 18 units on the graph of Figure 29. Inspection of Figure 29 shows that the predicted spike does indeed appear.

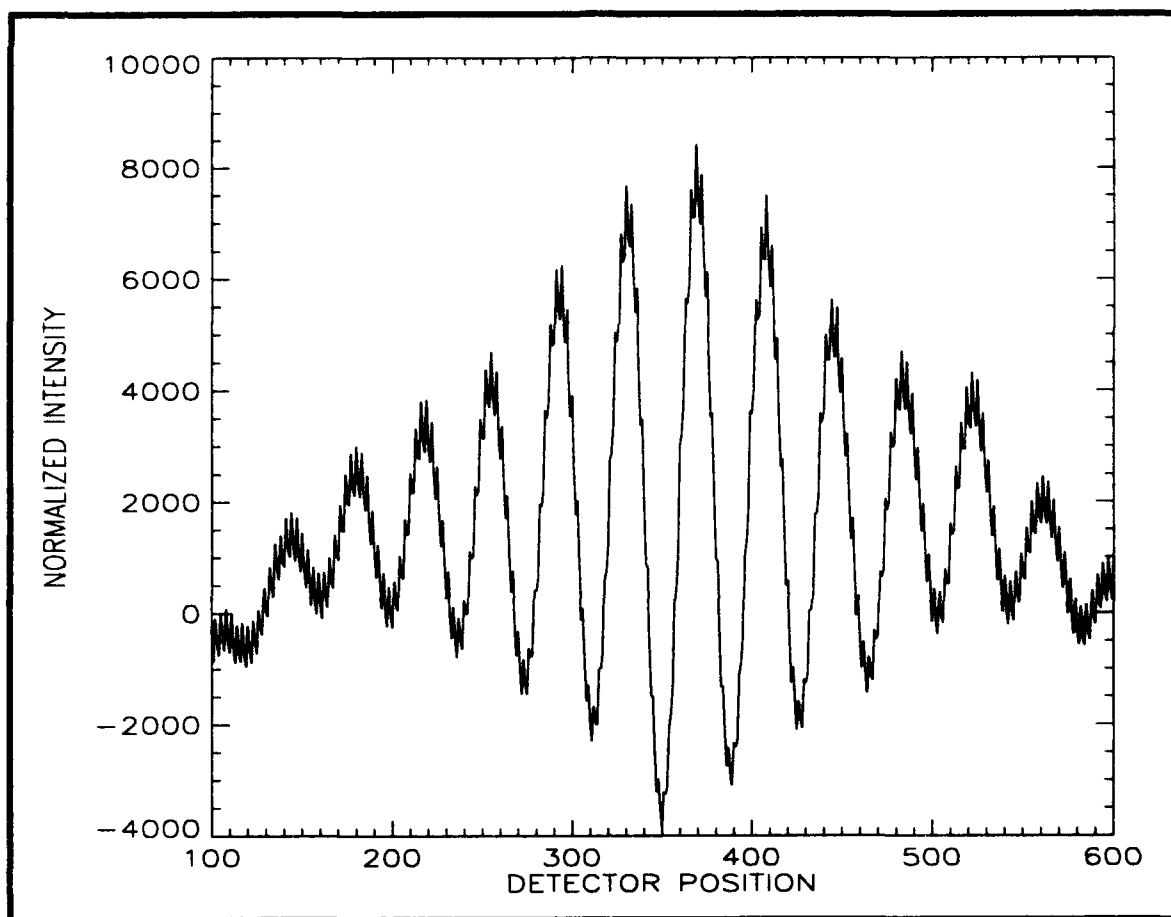


Figure 28 Interference Profile for Mercury Vapor Lamp (High Spatial Frequency)

Figures 26 and 29 show another interesting feature of the AMI. As spatial frequency increases and the distance from the tuned wavelength increases, the intensity of the peak decreases.

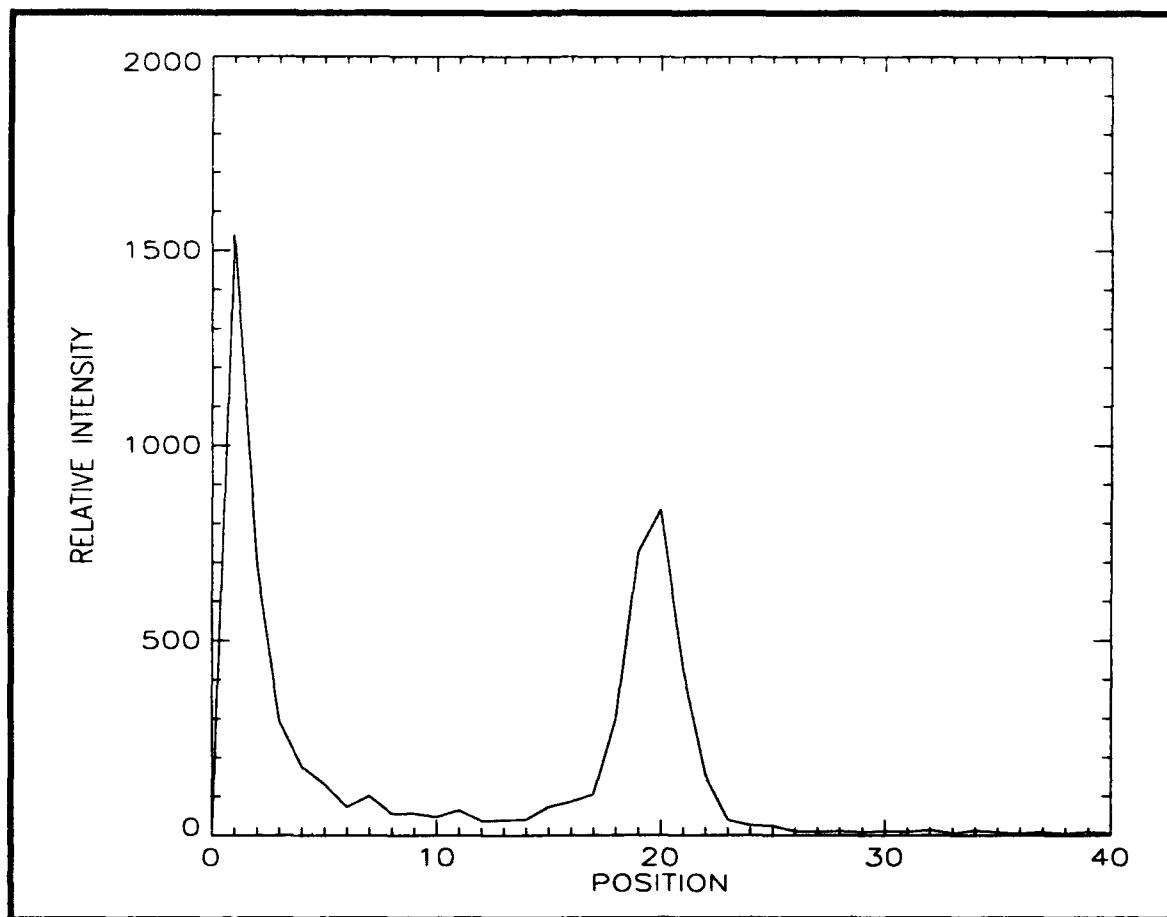


Figure 29 Fourier Transform for Mercury Vapor Lamp (High Spatial Frequency)

Figure 30 illustrates this effect. The three curves plotted on the graph were recorded using the mercury vapor lamp as the light source. The only difference between the curves is that they correspond to different spatial frequencies. Curve A was plotted for an interference pattern that contained 11 bright fringes. Curves B and C show interference patterns with 20 and 29 bright fringes, respectively. Figure 30 clearly displays the relationship between spatial frequency and intensity. As frequency increases, the intensity of the peaks drop from 1600 for Curve A, to 900 for Curve B, to 300 for Curve C. As a result, this becomes an important design consideration

when determining the tuned wavelength for the AMI. If λ_0 is too far from the oxygen 1304.86-Å line, the intensity of the profile might be too low to accurately reconstruct the spectrum.

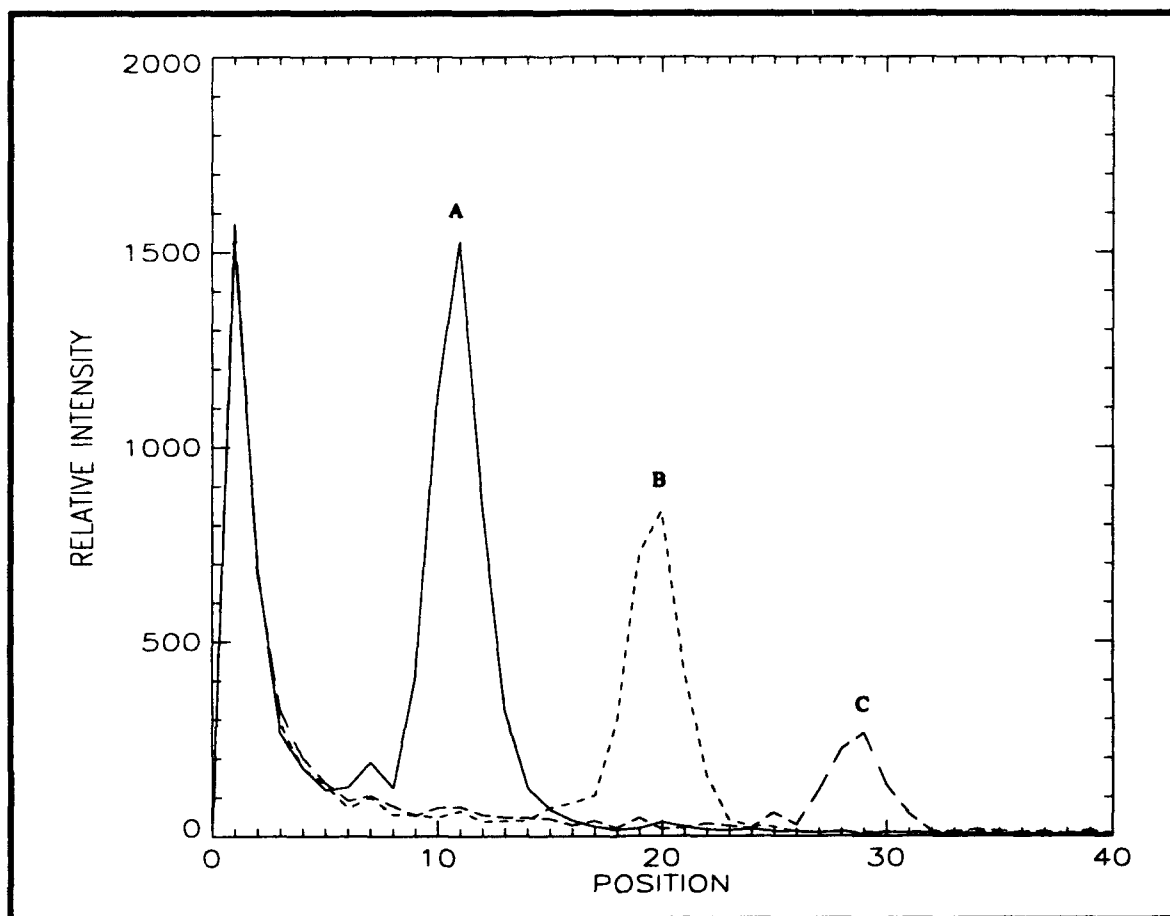


Figure 30 Plot of Intensity Versus Spatial Frequency (Mercury Vapor Lamp)

C. TESTING WITH SODIUM VAPOR LAMP

The next phase in testing the interferometer design was to verify the performance of the instrument using a different, less intense light source. sodium was chosen because it exhibits a doublet emission at a wavelength of 5889-Å, which is less intense than either the He-Ne laser tested by Risley (1992) or the mercury vapor lamp examined previously. The nature of the doublet emission (two distinct emission lines within 9-Å of each other) also provided a unique

opportunity for testing the AMI. Not only could the performance of the interferometer be verified with low intensity sources, the resolving power of the instrument could also be examined.

The resolution limit and bandwidth of the instrument for the sodium doublet emission can be determined from Equation (16) and Figure (14). Using

$$\Delta\theta = \tan^{-1} \frac{\lambda / 4}{L / 2} = \tan^{-1} \frac{2\lambda}{L} = \frac{2\lambda}{L}, \quad (35)$$

for the doublet emission, Equation (16) becomes

$$\Delta\lambda_{\min} = \frac{2a \cos(\theta) \lambda}{L}. \quad (36)$$

With $L=8.7$ mm, $a=4.1667 \times 10^{-4}$ mm/line ($1/\rho$), $\theta=28.5^\circ$ and $\lambda=5889\text{-}\text{\AA}$ for the sodium lamp, $\Delta\lambda_{\min}=0.2487\text{-}\text{\AA}$. Since the doublet emission lines are separated by approximately $9\text{-}\text{\AA}$, the resolving power is $\lambda/\Delta\lambda_{\min}=72$ pixel units.

The bandwidth (BW) can be determined using the Nyquist sampling criteria, which requires a minimum of two samples per cycle. Therefore

$$BW = \left(\frac{N}{2} \right) \Delta\lambda_{\min}, \quad (37)$$

where N is the number of detector elements. With $N=753$, $BW=93.6\text{-}\text{\AA}$.

After completing the numerical analysis, the mercury bulb in the Oriel lamp was replaced with a sodium vapor bulb. Since the sodium lamp operated at a slightly different wavelength, the instrument was realigned visually so that both beams again intersected at the detector. As before, once the mirrors were properly oriented it only took a few minutes to establish an interference pattern and fine tune the image. Figure 31 is a picture of the resulting interference pattern.



Figure 31 Interference Pattern for Sodium Vapor Lamp (λ_0 less than λ_1 and λ_2)

The image of Figure 31 clearly shows two superimposed interference patterns. The pattern with four or five fairly wide bright fringes is the more dominant of the two and is a result of the emission line which is nearest λ_0 . The other pattern, with approximately 55 narrow fringes, results from the emission line farthest away from λ_0 . For future reference, the two emission lines from the sodium vapor lamp are designated as λ_1 and λ_2 . Since the mirrors were aligned visually and not to any particular wavelength, there was no way of telling from Figure 31 where λ_1 and λ_2 lay in relation to λ_0 . A relatively simple method, and the one used throughout the remainder of this thesis, was to adjust the AMI so that one of the interference patterns

completely disappeared. When one of the patterns disappeared, the instrument was tuned for that exact wavelength. By trial and error, it was then a simple matter to determine if the tuned wavelength was outside or between the sodium doublet emission lines. The data of Figure 31 was recorded for λ_0 less than λ_1 and λ_2 .

The only difficulty which arose while testing the sodium lamp was vertically aligning both interference patterns simultaneously. When one pattern was aligned the other was slightly askew and vice versa. After a number of attempts, the effort to align both patterns at the same time was abandoned and the patterns were lined up as close to vertical as possible. The interference profile for the image of Figure 31 is shown in Figure 32.

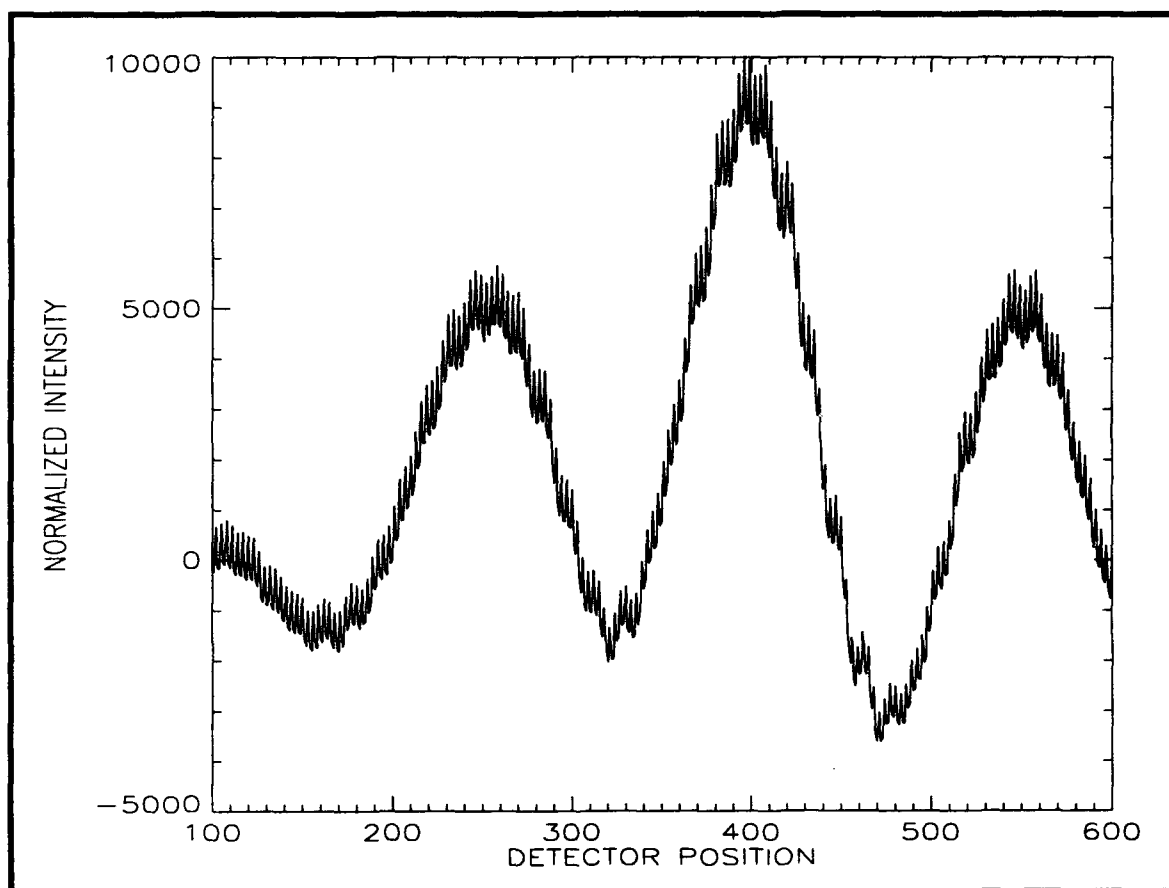


Figure 32 Interference Profile for Sodium Vapor Lamp (λ_0 less than λ_1 and λ_2)

As with Figure 31, the profile of Figure 32 also reflects the influence of two separate and distinct wavelengths. The wavelength with the lower spatial frequency gives the curve its general shape while the wavelength with the higher spatial frequency gives the curve its jagged transitions.

Figure 33 plots the Fourier transform of Figure 32. Contrary to our expectations, Figure 33 does not show two emission peaks.

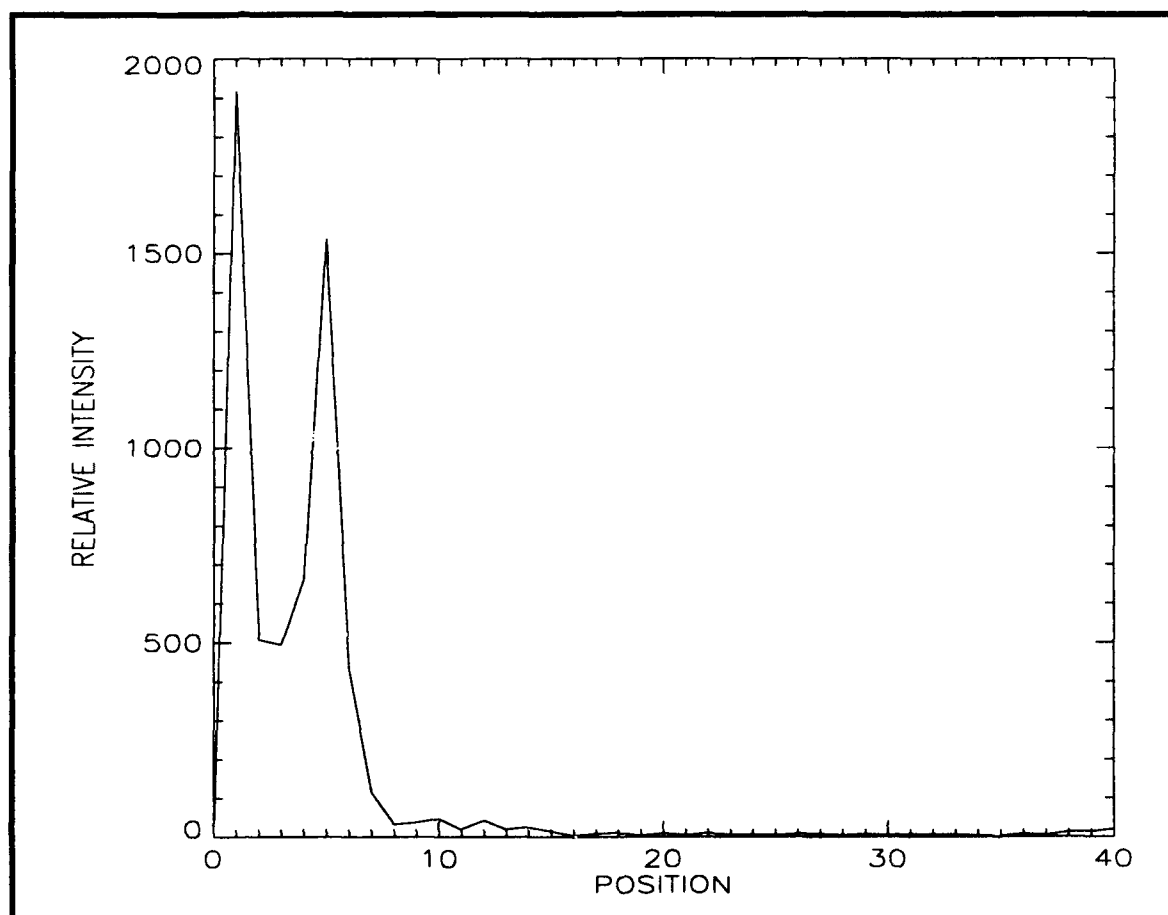


Figure 33 Fourier Transform for Sodium Vapor Lamp (λ_0 less than λ_1 and λ_2)

For some unknown reason the second peak was not visible even though two distinct spatial frequencies can be discerned in Figures 31 and 32. Although the data from the mercury

lamp indicates that the intensity should decrease with increasing spatial frequency, at a distance of around 30 to 40 pixel units some type of peak should be visible. In order to determine the reason only one peak was apparent, a number of runs were conducted for different tuned wavelengths. The AMI was adjusted and data recorded for the following situations: λ_0 on one side of λ_1 and λ_2 , λ_0 between λ_1 and λ_2 and λ_0 on the other side of λ_1 and λ_2 . Figure 34 illustrates the case where λ_0 is approximately midway between λ_1 and λ_2 .



Figure 34 Interference Pattern for Sodium Vapor Lamp (λ_0 between λ_1 and λ_2)

As in the case of Figure 31, the pattern of Figure 34 also shows two superimposed interference patterns. The fringes of Figure 34, however, are approximately the same width since

λ_0 is almost the same distance from λ_1 and λ_2 . Figure 35 is a plot of the interference profile for the image of Figure 34. Again, two wavelengths are visible on the interference profile.

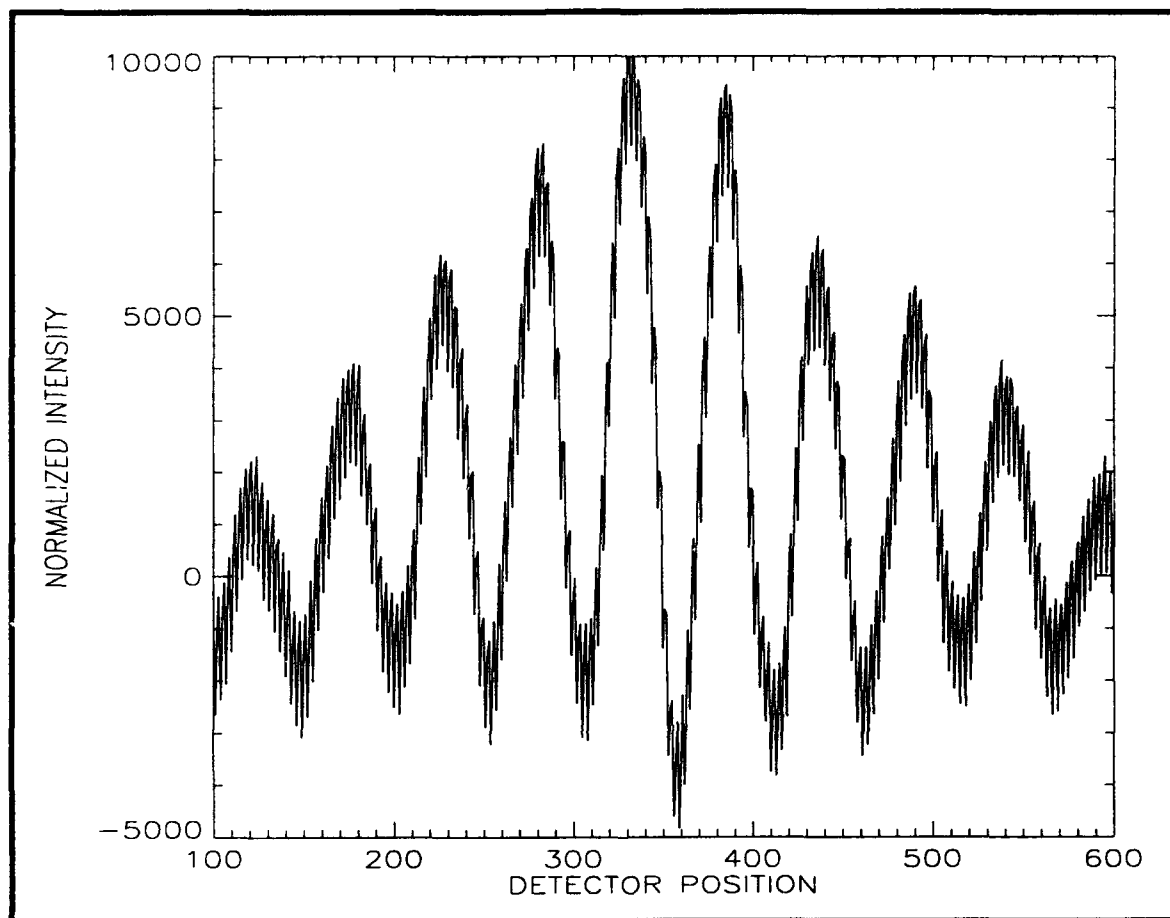


Figure 35 Interference Profile for Sodium Vapor Lamp (λ_0 between λ_1 and λ_2)

The graph of Figure 36 displays the Fourier transform of Figure 35. This time there does seem to be a faint second peak around pixel 36. The peak is too faint however, to say positively that it is a product of the second emission line. In all, ten runs were conducted but the data for all ten runs was inconclusive. Since the instrument seemed to be working properly and the second emission line was visible in the interference patterns and interference profiles, there had to be some other reason it was not appearing in the Fourier transform.

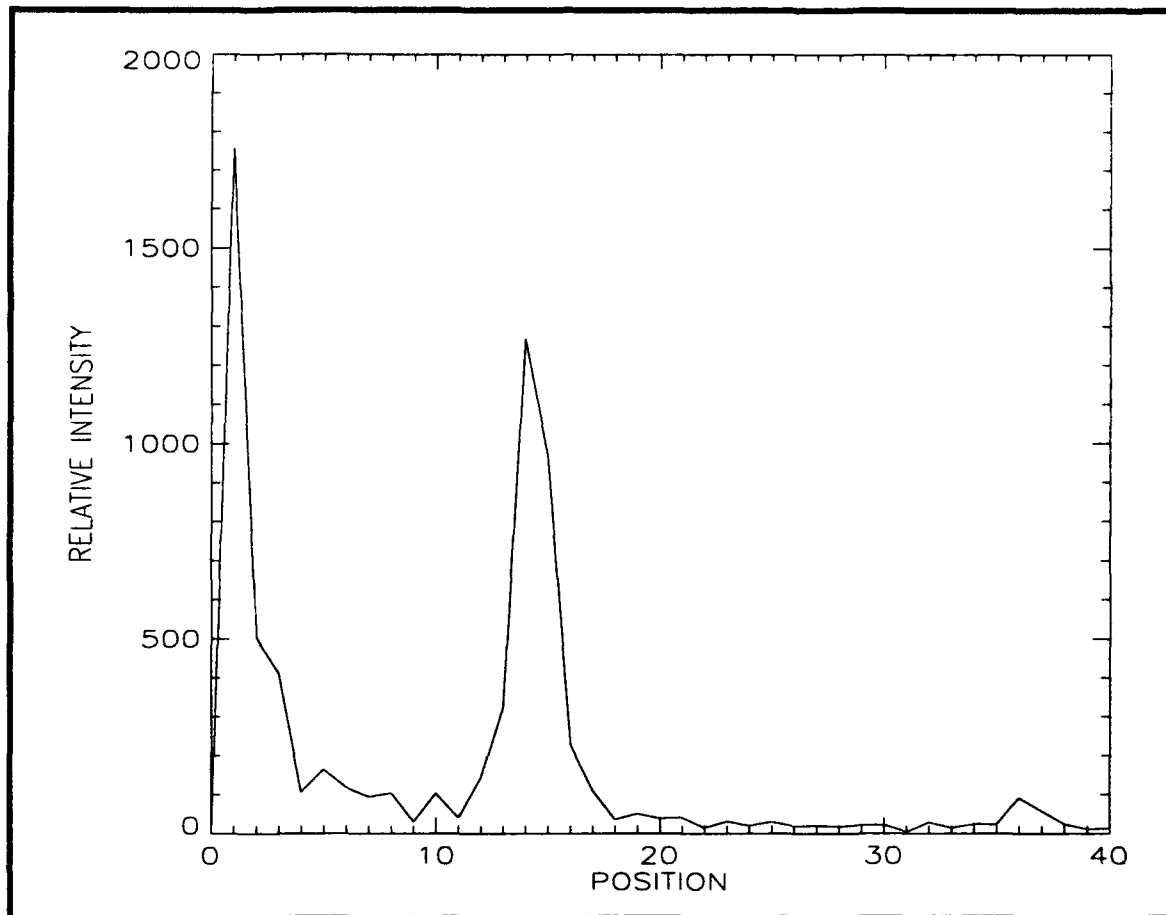


Figure 36 **Fourier Transform for Sodium Vapor Lamp (λ_0 between λ_1 and λ_2)**

One possible answer was the methodology used to analyze the raw data. The interference profiles were obtained by summing the intensities vertically (over all 244 vertical pixels) and then taking the Fast Fourier Transform (FFT). As noted previously though, the fringes were never perfectly vertical. When the fringes for λ_1 were vertical, the fringes for λ_2 were slightly tilted. To compensate for this, the array was summed by rows of two instead of 244 rows at once. In other words, the intensities for two rows were summed, then the FFT was taken for those two rows. After this step was completed, the resulting 122 FFT's were summed to create the final

Fourier transform array. The IDL procedure used to sum the array over a certain number of rows at once is listed in Appendix A.

Summing the array two rows at a time had a dramatic effect on the data. The second emission peak was clearly evident for all ten runs. The results of this analysis are listed in Table 3.

TABLE 3 SODIUM DOUBLET EMISSION ANALYSIS (Summed by Rows Of 2)

Run	λ_0 Position	λ_1 Pixel Distance	+ or -	λ_2 Pixel Distance	Total Separation
1	$\lambda_1 < \lambda_0 < \lambda_2$	14	+	36	50
2	$\lambda_1 < \lambda_0 < \lambda_2$	7	+	43	50
3	$\lambda_0 < \lambda_1 < \lambda_2$	12	-	63	51
4	$\lambda_1 < \lambda_2 < \lambda_0$	5	-	55	50
5	$\lambda_0 < \lambda_1 < \lambda_2$	4	-	55	51
6	$\lambda_1 < \lambda_0 < \lambda_2$	7	+	43	50
7	$\lambda_1 < \lambda_2 < \lambda_0$	4	-	54	50
8	$\lambda_1 < \lambda_0 < \lambda_2$	18	+	33	51
9	$\lambda_1 < \lambda_0 < \lambda_2$	25	+	25	50

The results listed in Table 3 are fairly consistent. The data shows that, regardless of the location of the tuned wavelength, the instrument displays an average spacing between the doublet emission lines of 50 pixel units. In fact, the experimentally determined resolution of 50 units compares favorably with the predicted resolving power of 72 units which was determined theoretically at the beginning of this section. This brings up an interesting point. When the resolving power was first determined theoretically, there was a mistake in Equation (36) and the resolving power was erroneously calculated as 36 units. After the runs were completed and the resolving power came out experimentally as 50 units, the equations were rederived, the algebra mistake was corrected, and the right theoretical value was determined to be 72 pixel units.

The findings of Table 3 bring up an interesting question. Namely, over how many rows should the data be summed to provide maximum definition between the peaks and the background noise? To answer this question the data from one particular run was examined. Run 1 was chosen arbitrarily and the intensity profile was summed over 1 row, 4 rows, 16 rows, 64 rows and 244 rows. The resulting five curves were then plotted and compared on the graph of Figure 37. Figure 37 shows that the definition between the second peak and the background noise improves steadily as the intensity distribution is summed up to about 64 rows at a time. At that point, the intensity of the second peak starts to decrease and it becomes harder to distinguish the peak from the background noise. Examination of other stored EDC files using this technique revealed the same general trend. Definition between the peak and background noise improved until the data was summed over approximately 32 to 64 rows at a time, then the definition started to decrease until the peak was indistinguishable from the background noise. The reason or reasons for this are not clearly understood at this time.

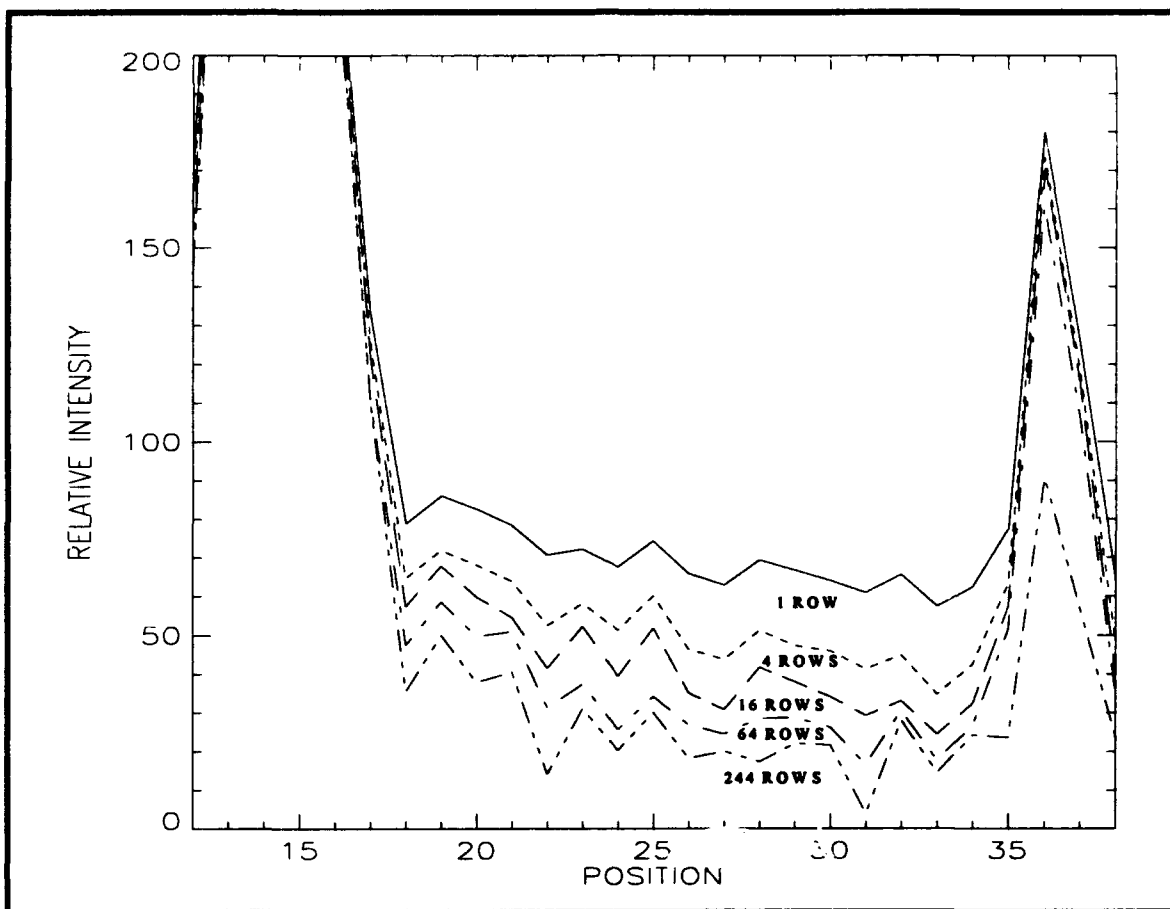


Figure 37 Comparison of Sodium Doublet Emission Profiles (Intensity Profile Summed Over 1, 4, 16, 64 and 244 Rows)

D. FINAL MODIFICATION OF AMI

Validation of the prototype instrument as a tool to perform high resolution analysis of emission line profiles was finally complete. The only task that remained was to perform a slight modification to the prototype so that it reflected a design more suitable for operation in the vacuum ultraviolet. This was accomplished by removing the focusing lens and replacing the pinhole opening with a narrow slit. Removing the focusing lens between the light source and aperture enabled the instrument to collect any incident light within the geometric window of the slit-parabolic mirror configuration and gave the AMI a wide field of view. A slit was used in

place of the pinhole opening because it was easier to adjust the width of the slit and to control the amount of light striking the off-axis mirror.

The AMI, with modifications complete, is pictured in Figures 38 and 39. Figure 38 shows the front view of the instrument as seen from behind the detector. Figure 39 displays the rear view of the instrument viewed from behind the diffraction grating. The light source shown in Figures 38 and 39 is the Oriel lamp with mercury vapor bulb. The mercury lamp was used temporarily to adjust the various optical elements and see what effect, if any, the modifications had on AMI performance.

In the front view of Figure 38, the zero order mirror (mounted on adjustable base) is the element in the left foreground of the picture. Directly behind the mirror is the diffraction grating mounted in its circular holder. To the right of the zero order mirror is the solid state detector with the computer cable attached to rear. Next to the detector is the minus one order mirror. The off-axis parabolic mirror with its polished surface can be seen in the background. The elements farthest to the right of the picture are the slit and, directly in front of it, the mercury lamp.

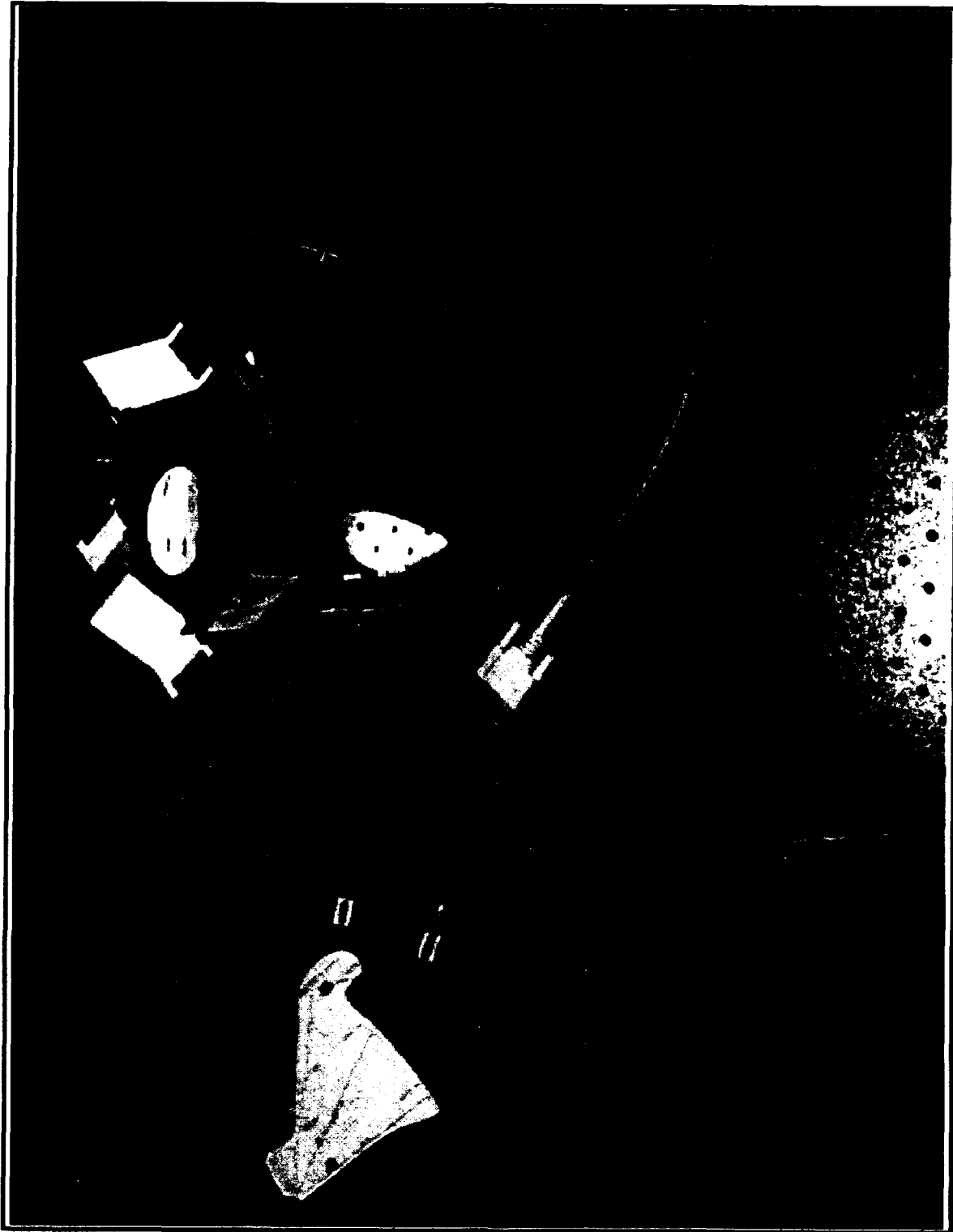


Figure 38 Front View of AMI

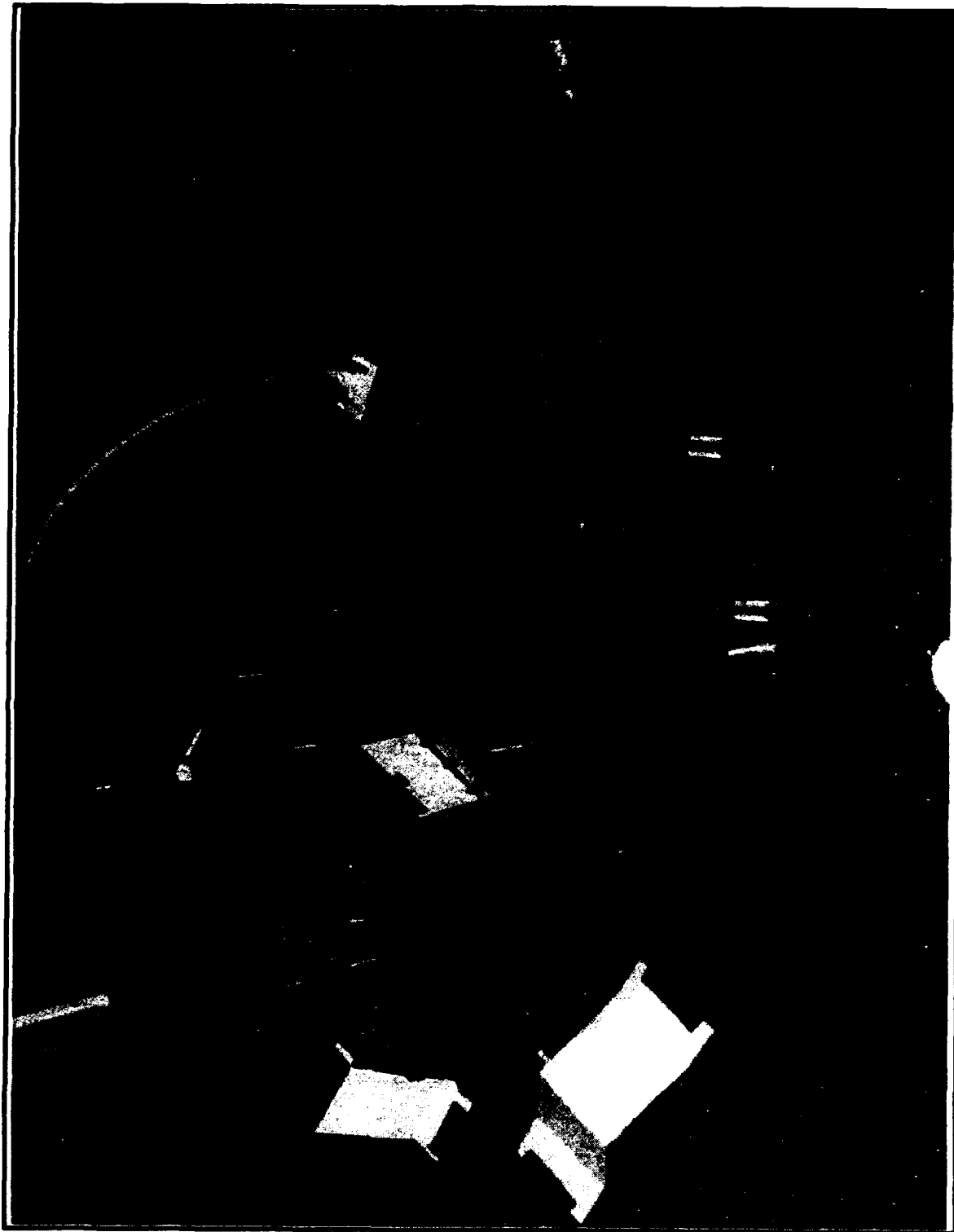


Figure 39 Rear View of AMI

The slit itself can be seen in the rear view of Figure 39. The circular mirrors and detector opening are also visible. Another feature evident in the rear view of Figure 39 is the spacing between the diffraction grating and reflecting mirrors. The mirrors are situated as close to the grating as the base will allow. Tests showed that the distance between the grating and mirrors had no visible effect on AMI performance. In fact, the ability to fit the instrument in virtually any size container is one of its main advantages.

Figure 40 shows an interference pattern recorded after final modifications to the AMI were completed. Figure 40 was taken with the mercury lamp and an exposure time of 500 msec. The interference pattern is not as distinct in Figure 40 as in previous figures because of the light intensity reaching the detector. Since the light source was directly in front of the slit, the amount of light reaching the detector was much higher and tended to wash out the picture. Even at half the exposure time (500 msec versus 1000 msec for other figures) it was difficult to get a clear pattern. This is another item to consider when building an instrument for actual use. The best performance can be achieved by placing a reflector or another off-axis mirror in front of the aperture to control the distribution and intensity of light reaching the detector.

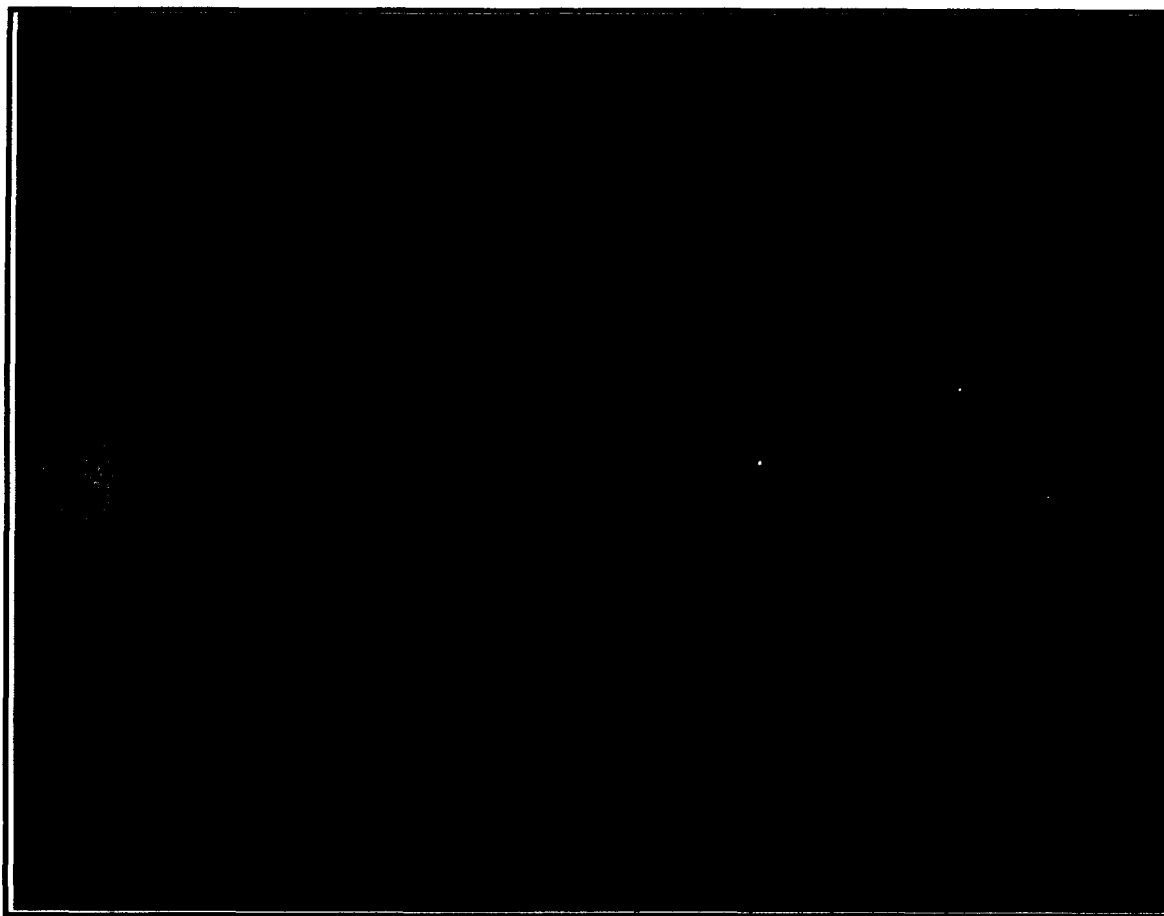


Figure 40 Interference Pattern after Final Modifications to AMI

E. TESTING WITH ULTRAVIOLET SOURCE

The ultimate goal of this thesis was to examine the feasibility of using the AMI as a high resolution instrument in the ultraviolet portion of the electromagnetic spectrum. The final phase of testing, therefore, required the use of a light source which operated in the ultraviolet wavelength range. After considerable thought, the mercury line at a wavelength of 2537-Å was chosen. The mercury line offered an intense source at a wavelength close to the minimum wavelength acceptable for the diffraction grating of the prototype instrument. Recall from Equation (20) that a wavelength of 2537-Å requires a grating with $\rho_{\min}=2628$ lines/mm. The

prototype grating had a density of 2400 lines/mm which, although not perfect, is still fairly close to optimum).

Operating the AMI in the ultraviolet range presented two problems. The first problem was moving and adjusting the mirrors with an ultraviolet source. Since the light from the UV source was not visible to the naked eye, the mirrors could not be aligned visually. Because of the change in wavelength, the reflecting mirrors had to be moved and realigned. Initial placement of the mirrors was accomplished using a computer template. The template, which was taped to the workbench, showed the position of the incident beam, the diffraction grating, the two plane mirrors and the output beam to the detector for an incidence angle of $\theta_i=45^\circ$.

The other problem which needed to be addressed was detecting the interference pattern. The computer camera did not operate in the UV range and required some modifications to detect light in that region of the spectrum. After careful consideration, an image intensifier was used to alleviate the problem. The image intensifier, a ITT model F4145 plate image intensifier, was bolted directly to the front of the solid state computer camera. Photons entering the intensifier strike a photocathode, causing electrons to be ejected and accelerated by a potential into a microchannel plate where they strike a phosphor screen. The phosphor screen emits visible light which is then detected by the camera. Power to the image intensifier was provided via a separate circuit and was adjustable from 0 to 15 volts.

Once modifications to the camera were complete, the mirrors were placed according to the template and power to the lamp and image intensifier was turned on. As expected, the zero order mirror was easy to align. The detector was used to check the placement of the minus one order mirror and showed that the template was an accurate indicator of the various reflection angles and mirror positions. The image intensifier seemed to work best for supply voltages

between 5 and 6 volts. Any power settings above 6 volts saturated the CCD camera. Final adjustments were accomplished by adjusting the zero and minus one order mirrors so that both the zero and minus one beams overlapped at the center of the detector. The setup worked so well that adjustments were completed for the UV source almost as fast as for the visible light sources. The only problem with the configuration was that the intensity of the zero order beam was five to ten times brighter than the minus one order beam. When power to the intensifier was adjusted for the minus one order beam, the zero order beam saturated the computer camera. The large difference in beam intensities eliminated any possibility of establishing an interference pattern.

The incidence angle was adjusted from 45° to 5° to try and shift some of the intensity from the zero beam to the minus one beam and equalize the beam intensities. This new setup shifted the configuration of the mirrors and detector so that the minus one order mirror was on one side of the incident beam and the zero order mirror and detector were on the other side of the beam. The new configuration worked better than expected and shifted too much of the intensity from the zero to minus one order beam. When power was adjusted for the zero beam the intensity of the minus one beam saturated the camera, again preventing the appearance of an interference pattern.

The next logical step was to balance the beam intensities by configuring the instrument for some incidence angle between 5° and 45° . The difficulty with this was that the $m=1$ beam and ultraviolet emission lines in the vicinity of $3000\text{-}\text{\AA}$ (also from the mercury lamp) interfered with the $m=0$ and -1 beams at the detector for most incidence angles between 5° and 45° . As a result, there was no usable incidence angle for the mercury lamp that equalized the intensities of the beams enough to create an interference pattern. One possible solution would be to use a diffraction grating with a higher ruling density so that more of the intensity is concentrated in the

$m=0$ and -1 beams. Unfortunately, no other gratings were immediately available and testing of the AMI in the ultraviolet region was discontinued.

V. SUMMARY, CONCLUSIONS AND RECOMMENDATIONS

A. SUMMARY OF FINDINGS

Over the course of this thesis, numerous experiments were conducted to validate the All-Reflection Michelson Interferometer as a high resolution, compact instrument for use in the EUV and FUV portion of the electromagnetic spectrum.

First, the instrument was examined using a mercury vapor lamp that operated at a wavelength of 5461-Å. Test results showed that the AMI operated exactly as predicted. Establishing an interference pattern at the detector took a matter of minutes and the device was easy to tune with minor adjustments to the minus one order mirror. The resulting interference patterns were analyzed using IDL procedures designed to produce interference profiles and Fourier spectrums. As expected, the Fourier transform of the interference profiles returned a monochromatic spectrum.

Next the prototype was operated using a sodium source that produced a doublet emission at a wavelength of 5889-Å. The doublet emission was chosen to test AMI performance with a non-monochromatic source and determine the resolving power of the instrument. Experiments revealed that the instrument operated equally well with a non-monochromatic source and the resolution of the instrument agreed fairly closely to theoretical predictions. For reasons not yet understood, the resolution of the emission peaks varied depending on the number of rows used to sum the intensities. The greatest definition between peaks occurred when the intensities were summed approximately 32 to 64 rows at a time.

The prototype was modified for operation in the ultraviolet and was tested using a mercury source with a wavelength of 2537-Å. Although an interference pattern was never established, some very useful information was gathered, including the efficacy of the image intensifier/CCD camera assembly for use as a detector in the ultraviolet portion of the spectrum.

There were two reasons an interference pattern was never generated using a UV source. First, there was interference from other diffraction orders and emission lines. Second, the difference in intensity between the beams precluded any pattern from forming. The first problem could be resolved by using a different source and the second problem could be eliminated by increasing the ruling density of the grating and determining the optimum incidence angle for the wavelength under observation.

The experiments conducted during this thesis provided some extremely useful information and validated the use of the AMI as a high resolution sensing instrument in the ultraviolet region. The optical elements are simple, lightweight and relatively inexpensive. The instrument in general is compact, is easy to tune and adjust and very reliable. Also, since the AMI has no moving parts, it is sturdy and should be fairly easy to construct.

B. RECOMMENDATIONS FOR FURTHER STUDY

With the successful testing of a functioning prototype complete, all future work should be concentrated towards the development of an actual flight instrument. The engineering development should focus on a number of important elements. First, different methods of collecting and collimating the incident light should be examined and tested. Second, the type and optimum grating density of the diffraction grating should be explored in more detail. Third, the methodology for mounting the optical elements to reduce vibrations due to shock and temperature fluctuations during flight should be investigated. Fourth, detectors suitable for

sensing interference patterns in the EUV and FUV region of the electromagnetic spectrum should be examined. Finally, a suitable arrangement (including dimensions, weight and placement of elements) to conform to sounding rocket or space vehicle payload constraints should be explored.

APPENDIX A **IDL PROCEDURES**

PRO INITVAL,T,WLSIG,WLOFF,WLCEN,I0,XSEC

; THIS PROCEDURE GIVES INITIAL VALUES FOR THE
; OXYGEN 1304 LINE PROFILE PROCEDURES

WLSIG=.0478D	; LINE DISPERSION(ANGSTROMS)
WLOFF=.0478D	; OFFSET OF EMISSION
PEAKS(ANGSTROMS)	
WLCEN=1304.86D	CENTER WAVELENGTH(ANGSTROMS)
I0=1D	; AMPLITUDE
A=15.9994D	; ATOMIC WEIGHT OF OXYGEN
	; ATOM(GRAMS)
F12=.0485D	; OSCILLATOR STRENGTH
XSEC=1.16D-14*WLCEN*F12*((A/T)^.5)	; RESONANT SCATTERING CROSS
	; SECTION(CM^2)
RETURN	
END	

PRO SOLARLIN,T,SOLINT,WL

; THIS PROCEDURE CALCULATES THE SOLAR OXYGEN 1304.86 LINE PROFILE

```

INITVAL,T,WLSIG,WLOFF,WLCEN,I0,XSEC
NPTS=2000
WL=DBLARR(4000)
SOLINT=DBLARR(4000)
WL=WLCEN-.25+FINDGEN(2*NPTS)/(NPTS*4)
SOLINT=I0*(EXP(-((WL-WLCEN+WLOFF)^2)/WLSIG^2)+EXP(-((WL-WLCEN-
WLOFF)^2)/WLSIG^2))
RETURN
END

```

PRO TERLIN,WL,TERESINT

; THIS PROCEDURE CALCULATES THE TERRESTRIAL 1304.86 LINE USING A
; DOPPLER LINE PROFILE

NPTS=2000
WLCEN=1304.86D
WL=WLCEN-.25+FINDGEN(2*NPTS)/(NPTS*4)
WLSIG=1.862E-6*WLCEN
TERESINT=EXP(-((WL-WLCEN)^2)/WLSIG^2)

RETURN
END

PRO VOITLIN,T,WL,VOIGTINT

; THIS PROCEDURE CALCULATES THE TERRESTRIAL 1304.86 LINE PROFILE BASED
; ON THE VOIGT FUNCTION

A=1.108D-2
WLCEN=1304.86D
FREQ=DBLARR(4000)
U=DBLARR(4000)
H=DBLARR(4000)
VOIGTINT=DBLARR(4000)
DOPWIDTH=2.47D8*SQRT(T)
FREQCEN=2.998D8/(WLCEN*1D-10)
FREQ=2.998D8/(WL*1D-10)
U=(FREQ-FREQCEN)/DOPWIDTH
H=VOIGT(A,ABS(U))
VOIGTINT=H/(DOPWIDTH^.5)*(!DPI^.5)

RETURN
END

PRO VOBSINT,T,COLDEN,WL,VOBSINT

; THIS PROCEDURE CALCULATES THE OBSERVED OXYGEN 1304.86 LINE PROFILE
; USING THE VOIGT FUNCTION TO MODEL THE TERRESTRIAL LINE

INITVAL,T,WLSIG,WLOFF,WLCEN,I0,XSEC
SOLARLI,T,WLSIG,WLOFF,WLCEN,I0,SOLINT,WL
VOITLIN,T,WL,VOIGTINT
VOBSINT=DBLARR(4000)
VOBSINT=SOLINT*EXP(-(COLDEN*XSEC*VOIGTINT))

RETURN
END

PRO INTVSCOL,T,COLDEN,INT

; THIS PROCEDURE CALCULATES THE NORMALIZED INTENSITY OF THE
; OBSERVED OXYGEN 1304.86 LINE VERSUS AN ARRAY OF COLDENS

INITVAL,T,WLSIG,WLOFF,WLCEN,I0,XSEC
COLDEN=FLTARR(101)
INT=FLTARR(101)
COLDEN(0)=1E16

FOR J=1,100 DO BEGIN
COLDEN(J)=COLDEN(J-1)*1.26
ENDFOR

FOR J=0,100 DO BEGIN
VOBSINT,T,COLDEN(J),WL,VOBSINT
INT(J)=TOTAL(VOBSINT)
ENDFOR

INT=INT/INT(0)

RETURN
END

PRO INTVCOL1

; THIS PROCEDURE PLOTS THE GROWTH CURVE OF THE OXYGEN 1304.86 LINE
; SEVERAL TEMPS AND SENDS THE DATA TO A CGM FILE

```
SET_PLOT,'CGM'  
DEVICE,FILENAME='GROWTH.CGM'  
INTVSCOL,300,COLDEN,INT  
PLOT_OI,COLDEN,INT,XSTYLE=1,XRANGE=[1E16,1E24],$  
XTITLE='COLUMN DENSITY (CM^-2)',  
YTITLE='INTENSITY RATIO (Iobserved/I solar)'  
OPLOT,[1E17,1E18],[.35,.35]  
XYOUTS,5E18,.35,'T=300K',SIZE=.75  
OPLOT,[1E17,1E18],[.3,.3],LINE=1  
XYOUTS,5E18,.3,'T=600K',SIZE=.75  
OPLOT,[1E17,1E18],[.25,.25],LINE=2  
XYOUTS,5E18,.25,'T=900K',SIZE=.75  
OPLOT,[1E17,1E18],[.2,.2],LINE=3  
XYOUTS,5E18,.2,'T=1200K',SIZE=.75  
OPLOT,[1E17,1E18],[.15,.15],LINE=4  
XYOUTS,5E18,.15,'T=1500K',SIZE=.75  
OPLOT,[1E17,1E18],[.1,.1],LINE=5  
XYOUTS,5E18,.1,'T=1800K',SIZE=.75
```

```
FOR T=600,1800,300 DO BEGIN  
  INTVSCOL,T,COLDEN,INT  
  OPLOT,COLDEN,INT,LINE=(T-300)/300  
ENDFOR
```

```
DEVICE,/CLOSE  
SET_PLOT,'WIN'
```

```
RETURN  
END
```

PRO IMAGE,FILE,IMAGE

**; THIS PROCEDURE READS TIFF FILES PRODUCED BY THE EDC CAMERA AND
; SENDS THE PICTURE TO THE SCREEN**

**FILENAME='C:\EDC\' + FILE
IMAGE=TIFF_READ(FILENAME)
LOADCT,6
TV,IMAGE,4,8**

**RETURN
END**

PRO PROFILE,FILE,PROF

**; THIS PROCEDURE READS TIFF FILES PRODUCED BY THE EDC CAMERA AND
; SUMS THE INTENSITIES BY COLUMN TO PRODUCE AN INTERFERENCE PROFILE**

**FILENAME='C:\EDC\' + FILE
IMAGE=TIFF_READ(FILENAME)
PROF=TOTAL(IMAGE,2)
PROF=PROF-TOTAL(PROF*1.)/753.**

**RETURN
END**

PRO SPECTRUM,FILE,PROF,SPEC

**; THIS PROCEDURE READS TIFF FILES PRODUCED BY THE EDC CAMERA, SUMS
; THE INTENSITIES BY COLUMN TO PRODUCE AN INTERFERENCE PROFILE AND
; TAKES THE FOURIER TRANSFORM**

**FILENAME='C:\EDC\' + FILE
IMAGE=TIFF_READ(FILENAME)
PROF=TOTAL(IMAGE,2)
PROF=PROF-TOTAL(PROF*1.)/753.
SPEC=ABS(FFT(PROF,-1))**

**RETURN
END**

PRO GETSPEC,FILE,NUM,SPEC

```
; THIS PROCEDURE READS DATA FROM A TIFF FILE USING THE IMAGE  
; PROCEDURE, SUMS THE DATA NUM ROWS AT A TIME, TAKES THE FOURIER  
; TRANSFORM OF THE PROFILE AND STORES THE DATA AS A RECORD IN THE  
; FILE NEWSPEC.DAT
```

```
SPEC=FLTARR(753)  
FDAT=FLTARR(753)  
IMAGE,FILE,IMAGE  
FINISH=FIX(244./NUM)-1
```

```
FOR J=0,FINISH DO BEGIN  
  DAT=TOTAL(IMAG(*,NUM*J:NUM*J+(NUM-1)),2)  
  FDAT=ABS(FFT(DAT-TOTAL(DAT)/753.,-1))  
  SPEC=SPEC+FDAT  
ENDFOR
```

```
IF NUM*J+(NUM-1) LE 244 THEN BEGIN  
  DAT=TOTAL(IMAG(*,NUM*J:*),2)  
  FDAT=ABS(FFT(DAT-TOTAL(DAT)/753.,-1))  
  SPEC=SPEC+FDAT  
ENDIF
```

```
RETURN  
END
```

APPENDIX B

EDC FILES USED IN FIGURES

IMAGE8.TIF	Figure 24, Figure 25, Figure 26
IMAGE12.TIF	Figure 30
IMAGE14.TIF	Figure 27, Figure 28, Figure 29, Figure 30
IMAGE15.TIF	Figure 30
IMAGE26.TIF	Figure 31, Figure 32, Figure 33
IMAGE32.TIF	Figure 34, Figure 35, Figure 36, Figure 37
IMAGE39.TIF	Figure 40

LIST OF REFERENCES

- Atkinson, J. D., IV, *Implementation and Use of a Computational Ray-Tracing Program for the Design and Analysis of Complex Optical Systems*, Master's Thesis, Naval Postgraduate School, Monterey, California, March 1993.
- Carlson, Scott M., *Validation of the Design of a High Resolution All-Reflection Michelson Interferometer for Atmospheric Spectroscopy*, Master's Thesis, Naval Postgraduate School, Monterey, California, June 1993.
- Cleary, D. D., Nichols, J., and Davis, D. S., *Design for an All-Reflection Michelson Interferometer*, *Applied Optics*, 31, 433, 1992.
- Gladstone, G. R., *Solar OI 1304.86 Å Triplet Line Profiles*, Earth and Planetary Atmospheres Group, Space Science Laboratory, University of California, Berkeley, 92JA00991, 1992.
- Harlander, J., Roesler, F. L., Chakbarti, S., *Spatial Heterodyne Spectroscopy: A Novel Interferometric Technique for the FUV*, *Proceedings of the SPIE*, 1344, 1990.
- Hecht, E., *Optics*, Addison Wesley Publishing Co., Reading, Massachusetts, 1987.
- Kruger, R. A., Anderson, L. W., Roesler, F. L., *All-Reflection Interferometer for Use as a Fourier-Transform Spectrometer*, *Journal of the Optical Society of America*, 62, 938, 1972.
- Meier, R. R., Feldman, U., Brown, C. M., Picone, J. M., *Absolute O and O₂ Concentrations in the Thermosphere from Skylab Occultation Data*, *Planet, Space Sci.*, 40, 8, 1992.
- Müller, K. D., *Optics*, University Science Books, Mill Valley, California, 1988.
- Nichols, J., *The Design of a New Far Ultraviolet Interferometer for Ionospheric Spectroscopy*, Master's Thesis, Naval Postgraduate School, Monterey, California, December 1990.
- Rybicki, G. B., Lightman, A. P., *Radiative Processes in Astrophysics*, John Wiley & Sons, Inc., New York, 1979.
- Wallace, Kenneth M., *Design of a High Resolution Spatial Heterodyne Interferometer*, Master's Thesis, Naval Postgraduate School, Monterey, California, December 1992.

INITIAL DISTRIBUTION LIST

- | | | |
|----|--|---|
| 1. | Defense Technical Information Center
Cameron Station
Alexandria, Virginia 22304-6145 | 2 |
| 2. | Library, Code 52
Naval Postgraduate School
Monterey, California 93943-5002 | 2 |
| 3. | Dr. William B. Colson, Chairman PH
Physics Department
Naval Postgraduate School
Monterey, California 93943-5000 | 1 |
| 4. | Dr. D. D. Cleary, Code PH/CI
Physics Department
Naval Postgraduate School
Monterey, California 93943-5000 | 3 |
| 5. | Lt Michael W. Gill
2901 17 Mile Drive
Pebble Beach, California 93953 | 1 |